Petroleum Science 23 (2026) 2991–3016

Contents lists available at ScienceDirect

Petroleum Science

journal homepage: www.keaipublishing.com/en/journals/petroleum-science

Original Paper

# Paleoenvironmental and paleoclimatic evolution of the Piçarras Formation, Santos Basin, Brazil, from cuttings and well logs

Jean Carlos Amorim[a,b,*], Filipe Vidal[a,b], Reiner Neumann[c,d], Carla Semiramis Silveira[a], Cleverson Guizan Silva[a], Fernando Freire[a], Victor Salgado-Campos[a]

[a] Departamento de Geologia e Geofísica, Instituto de Geociências, Universidade Federal Fluminense, Niterói, RJ 24210-346, Brazil
[b] Petróleo Brasileiro S.A. (Petrobras), Rio de Janeiro, RJ 20031-030, Brazil
[c] Centro de Tecnologia Mineral (CETEM), Rio de Janeiro, RJ 21941-908, Brazil
[d] Programa de Pós-graduação em Geociências, Museu Nacional, Universidade Federal do Rio de Janeiro (UFRJ), Rio de Janeiro, RJ 20940-040, Brazil

ARTICLE INFO

*Article history:*
Received 6 June 2025
Received in revised form
17 July 2025
Accepted 14 December 2025
Available online 17 December 2025

Edited by Xi Zhang and Jie Hao

*Keywords:*
Pre-salt
Mineralogy
Clay mineralogy
Lithogeochemistry

ABSTRACT

Reconstructing syn-rift paleoenvironmental systems requires an understanding of the complex interplay among tectonics, climate, and lacustrine sedimentation, which is crucial for petroleum exploration. The Piçarras Formation, deposited during the Barremian in the Santos Basin, offshore Brazil, constitutes a significant example of an alkaline lacustrine environment shaped by tectonic subsidence and climatic variability. This study presents the first integrated petrographic, mineralogical, lithogeochemical, and geophysical analysis of the formation, based on cutting samples and well logs from the 1-BRSA-1363-RJS well. Eight lithologies were classified into Mg-clay-bearing and Mg-clay-free assemblages, each with distinct mineralogical and geophysical signatures. A key insight of this study is the identification of saponite, a trioctahedral smectite occurring exclusively at depths below 6000 m, which serves as a diagnostic Mg-clay mineral for the Piçarras Formation. Its presence is associated with high alkalinity, brackish lacustrine waters, and low-energy depositional settings, correlating with elevated MgO contents (up to 16.1%). Saponite influences geophysical responses, notably by increasing clay-bound water in NMR logs, lowering resistivity, and altering neutron and sonic log readings. The Piçarras Formation comprises laminated siliciclastic mudstones, lime mudstones, laminites, fragmented bioclastic packstones, and hybrid rocks, recording cycles between more arid periods characterized by carbonate deposition and less arid intervals marked by increased siliciclastic input. A sharp lithological and mineralogical transition defines the contact with the Itapema Formation, evidenced by the disappearance of saponite and shifts in geochemical trends, such as $SiO_2$ and MgO. Operationally, saponite's swelling properties pose significant challenges for drilling with water-based fluids. This work refines the paleoenvironmental understanding of the Piçarras Formation and offers insights critical for pre-salt exploration and drilling strategies.



## 1. Introduction

The Piçarras Formation represents the oldest known sedimentary succession within the Santos Basin, deposited in a rift setting intricately associated with the breakup of Gondwana and the subsequent opening of the South Atlantic Ocean (Riccomini et al., 2012; Chinelatto et al., 2020). However, its mineralogical, geochemical, and geophysical characteristics remain less explored compared to the overlying rift formations (Leite et al., 2020), limiting our understanding of its depositional environments and basin evolution.

The primary structural unit in most rift lakes is an asymmetrical half-graben, a basin in which a major bounding fault exists only on one side (the escarpment margin), while the opposite side, the flexural margin, shoals more gradually away from the main fault, resulting in shallower water depths and reduced sediment accumulation (Cohen,

* Corresponding author.
*E-mail addresses:* jcamorim@id.uff.br, jcamorim@petrobras.com.br (J.C. Amorim).

Peer review under the responsibility of China University of Petroleum (Beijing).

https://doi.org/10.1016/j.petsci.2025.12.022
1995-8226/

2003; Balázs et al., 2017). These basins are commonly bounded by steep escarpments on one margin and more gently dipping slopes on the other, reflecting the asymmetrical nature of their tectonic setting (Cohen, 2003; Andric et al., 2017; Balázs et al., 2017).

Although asymmetrical half-grabens characterize rift systems, only a portion of these structures actually host lakes (Cohen, 2003). Rift basins are strongly influenced by episodic faulting events that control the nature of sedimentary infill (Leeder and Gawthorpe, 1987; Frostick and Reid, 1989, 1990; Morley et al., 1990; Tiercelin, 1990; Martins-Neto, 2000; Gawthorpe and Leeder, 2000; Gawthorpe et al., 2003; Leppard and Gawthorpe, 2006; Balázs et al., 2017). However, due to the limited volume and water mass of these systems, many researchers consider climate change to be an equally important factor governing basin infill (Olsen, 1986, 1990; Scholz et al., 1990; Prosser, 1993; Carroll and Bohacs, 1999; Ilgara and Nemec, 2005; Samanta et al., 2016; Fu et al., 2019).

Rift successions predominantly comprise fluvial and lacustrine deposits that serve as valuable archives for reconstructing long-term climatic variations (Olsen, 1986; Johnson and Odada, 1996; Ashley and Renault, 2002). Sedimentation in these basins reflects complex interactions among tectonics, climate, and volcanism (Ashley and Renault, 2002). Within these sequences, clay mineral assemblages, when accurately distinguished between detrital and authigenic origins, serve as paleoenvironmental indicators (Deocampo, 2015; Pozo and Calvo, 2018). Similarly, carbonate deposits, sensitive to climatic, tectonic, and base-level changes, provide essential data for continuous paleoclimate reconstructions (Platt and Wright, 1991; Alonso-Zarza and Wright, 2010a, 2010b; Li et al., 2020; Gomes et al., 2020; Jewuła et al., 2023).

The presence of hydrocarbons in ancient rift systems has motivated significant research into modern and ancient rift lakes (Katz, 1953; Lambiase, 1990; Cohen, 2003). In Brazil, the discovery of giant pre-salt oil fields in the Santos Basin has positioned the region as one of the world's foremost hydrocarbon provinces (Souza and Sgarbi, 2019). Since 2006, increased attention has focused on rift deposits in Brazil's southeastern marginal basins, primarily targeting the upper syn-rift and sag sequences that host major reservoirs (Carlotto et al., 2017; Leite et al., 2020; Pedrinha and Artagão, 2024). In contrast, the lower syn-rift stratigraphic unit of the Santos Basin, the Piçarras Formation, has received comparatively less study due to its limited economic relevance, despite its significance as a record of the earliest syn-rift phase. No direct permeability data exist due to the pelitic nature of these rocks. However, Nuclear Magnetic Resonance (NMR) porosity data from well 1-BRSA-1363-RJS show 0–11.9% free fluid (in local, submetric intervals), 0–13.4% capillary-bound fluid, and 0–15% clay-bound water, reflecting poor reservoir quality in the Piçarras Formation.

The Piçarras Formation is regarded as a potential source rock for the hydrocarbon-bearing carbonate reservoirs of the Barra Velha and Itapema formations (Freitas et al., 2022). The type section of the Piçarras Formation was defined in well 1-BRSA-369A-RJS, where a 171-m interval was drilled between 5277 and 5448 m depth in the central Santos Basin (Moreira et al., 2007). Initially, it was described as comprising sandstones, siltstones, and shales containing “talc-stevensite” minerals deposited in lacustrine settings, with alluvial polymictic sandstones and conglomerates occurring in proximal zones (Moreira et al., 2007). These talc-stevensite-bearing sandstones are moderately to well-sorted arenites composed of magnesium-clay-coated grains cemented by calcitic micrite (Cupertino et al., 2023). Mg-clay particles occur as ooids, peloids, and intraclasts, predominantly within the medium- to fine-sand fraction (Leite et al., 2020).

Leite et al. (2020) described intercalations of redeposited stevensite and hybrid rocks, interpreted as resulting from gravity flows triggered by storms or tectonic events, along with bivalve occurrences. Such mixtures are genetically incompatible, as Mg-clay minerals form under highly alkaline conditions (Jones, 1986; Galán and Pozo, 2011; Tosca and Masterson, 2014; Pietzsch et al., 2018; Pozo and Calvo, 2018; Tutolo and Tosca, 2018; Chase et al., 2021), whereas certain bivalve species cannot reproduce under such conditions (Calabrese and Davis, 1970; Locke, 2008; Vonhof et al., 2013).

Current paleoenvironmental models propose deposition of the Piçarras Formation in alkaline lakes (Moreira et al., 2007; Leite et al., 2020; Osório-Sanabria, 2022) under predominantly arid climates (Chumakov et al., 1995; Dias, 2005; Boucot et al., 2013; Hay and Floegel, 2013), punctuated by periods of increased humidity (Leite et al., 2020). These fluctuations led to lake regressions, favoring shallow-water sedimentation, and transgressions into deeper brackish conditions (Osório-Sanabria, 2022). Siliciclastic input likely entered via hypopycnal flows and was deposited by suspension settling. High alkalinity promoted syngenetic deposition of Mg-clays and transformation of detrital precursors in low-energy settings (Leite et al., 2020).

Historically, subsurface geological data acquisition has been accomplished through the analysis of drilling cuttings (Carugo et al., 2013). The use of drilling cutting samples in scientific studies has often been overlooked in favor of conventional cores and rotary sidewall cores (SWC), driven by the misconception that data quality is inherently superior in cores (Craigie, 2018). This perception may be reinforced by the additional requirements for rigorous depth control techniques and increased attention to drilling fluid cleaning when working with cuttings. Nevertheless, precise depth referencing of cutting samples is achieved through robust methodologies that account for lag time, widely applied across the petroleum industry (Bourgoyne et al., 1986; Lapeyrouse, 2002; Mitchell et al., 2011). Despite these challenges, cutting samples provide critical insights into the mineralogical and geochemical properties of subsurface formations. Their smoothed geochemical profiles facilitate the identification of trends and chemo-stratigraphic boundaries, enabling continuous, large-scale modeling (Craigie, 2015, 2018). Several studies have successfully employed cutting samples as primary lithological data sources (Bertetti and Prikryl, 2003; Carugo et al., 2013; Carr et al., 2014; Stuckman et al., 2019; Kowalska et al., 2020; Vidal et al., 2022; França et al., 2023; Imbuzeiro et al., 2024).

This study represents the first investigation of the Piçarras Formation in well 1-BRSA-1363-RJS, utilizing cutting samples along with wireline (WL) and logging-while-drilling (LWD) geophysical logs, with the objective of characterizing the mineralogical, lithogeochemical, and geophysical properties of the unit. For the first time, multivariate statistical analysis of mineralogical, geochemical, and geophysical data is integrated with petrographic examination of drilling cuttings to reconstruct sedimentary provenance, paleoclimate, depositional environments, and to evaluate the nature of the contact between the Piçarras and Itapema formations.

## 2. Geological settings

The Santos Basin is located in the southeastern region of Brazil and currently encompasses an area of approximately 350000 km$^2$ (Fig. 1(a) and (b)). The basin is bounded by the Cabo Frio High to the north and the Florianópolis Platform to the south (Milani et al., 2000), and it overlies two types of basement rocks:

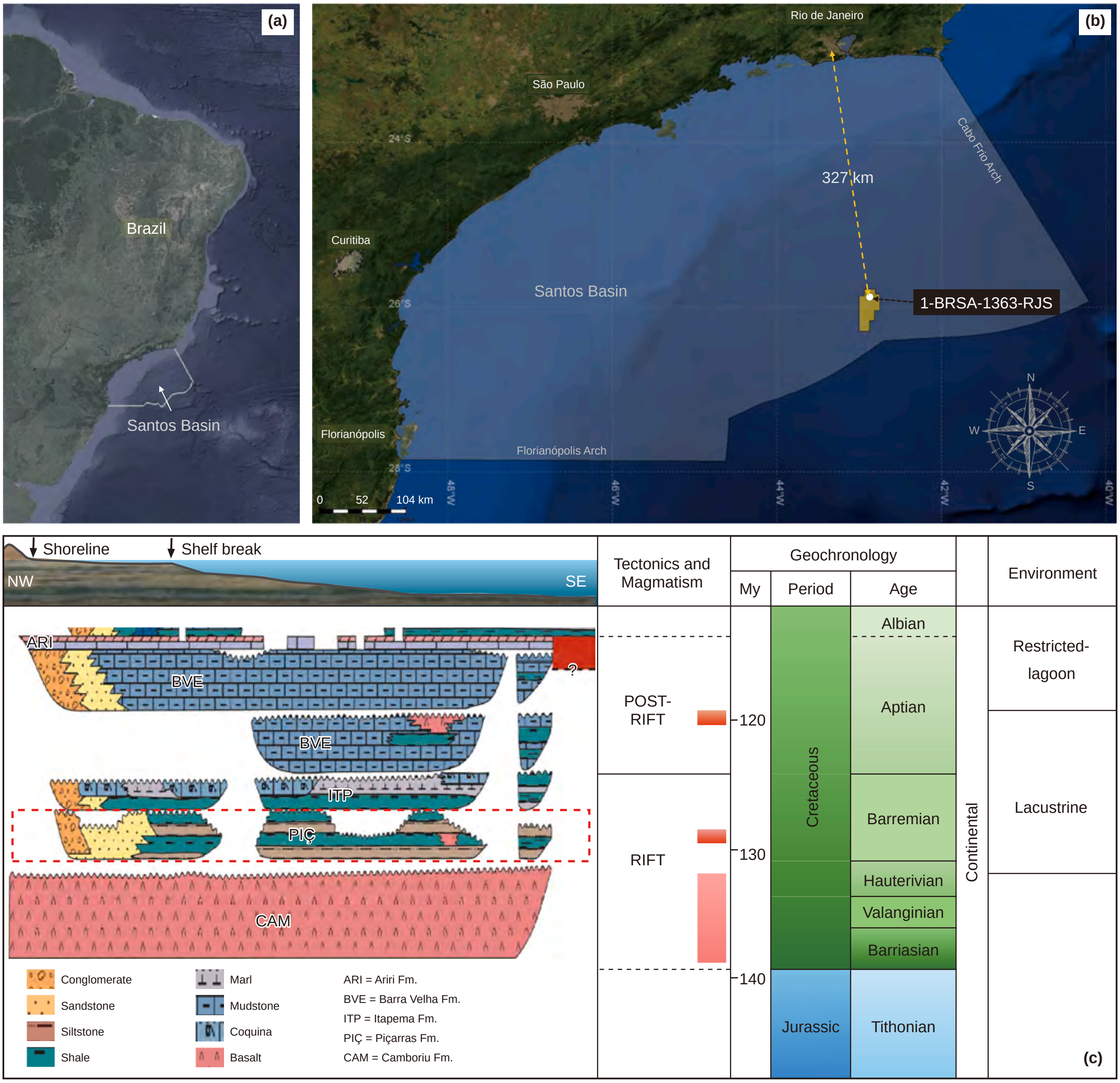


**Fig. 1.** Location and stratigraphic distribution of the Piçarras Formation. (**a**) Location map of the Santos Basin in the southeastern region of Brazil. (**b**) Location map showing the position of well 1-BRSA-1363-RJS. (**c**) Stratigraphic chart of the rift and post-rift sequences of the Santos Basin within the Pre-Salt interval (modified from Moreira et al., 2007).

a crystalline basement, composed mainly of Precambrian granitoids, gneisses, and metasediments, and a volcanic basement, consisting of basalts from the Camboriu Formation (Moreira et al., 2007).

The basin originated during the Early Cretaceous as a consequence of the breakup of the Gondwana Supercontinent. This tectonic event was preceded by extensive volcanic activity that resulted in the extrusion of basaltic flows, covering large areas of both Africa and South America (Conceição et al., 1988; Segev, 2002; Dias, 2005). The initial stages of rifting created half-grabens composed of faulted and rotated blocks, which were subsequently infilled with these igneous rocks, primarily basalts, forming the Camboriu Formation (Mizusaki et al., 1992; Leite et al., 2020). These volcanic deposits rest unconformably on the Precambrian crystalline basement, dominated by granitoids and gneisses (Moreira et al., 2007).

The widespread formation of rift basins linked to the fragmentation of Pangea, combined with intense volcanism and rapid seafloor spreading, profoundly reshaped global environmental conditions (Föllmi, 2012). These events drove climatic shifts between predominantly arid greenhouse states and transient humid intervals, with pronounced aridity during the Late Barremian and humidity rising during events such as the Taxy and Selli, spanning the latest Barremian to early Aptian (Föllmi, 2012).

During the Barremian stage, lacustrine sediments of the Piçarras Formation were deposited above the basaltic rocks of the Camboriu Formation (Fig. 1(c)), with an estimated age between 130 and 136.4 Ma (Moreira et al., 2007). This deposition was strongly controlled by structural activity during the rifting phase that led to the fragmentation of Gondwana (Milani et al., 2007; Leite et al., 2020). The upper boundary with the Itapema Formation (Fig. 1(c)) is marked by the Pré-Jiquiá (Intrabarremian)

Unconformity, with a maximum age of 126.4 Ma (Moreira et al., 2007). The Pré-Jiquiá Unconformity, although regionally named, corresponds to the global intra-Barremian unconformity and is recognized in other South Atlantic basins such as Gabon, Congo, Angola, and the Algarve Basin in Portugal (Moulin et al., 2005; Mendes et al., 2023). This lithological contact is characterized by significantly lower density log values, likely associated with the high magnesium clay content of the Piçarras Formation (Moreira et al., 2007; Leite et al., 2020). The Itapema Formation reflects a general decline in the alkalinity of the lacustrine system, which provided favorable conditions for bivalve proliferation (Leite et al., 2020). Such geological complexity underscores the importance of detailed stratigraphic, mineralogical, and geochemical investigations within this basin.

## 3. Materials and methods

This study utilized well log data and cutting samples provided by the Brazilian National Agency for Petroleum, Natural Gas and Biofuels (ANP), acquired from the 1-BRSA-1363-RJS well, drilled between 2018 and 2019 in the Peroba prospect, Santos Basin, approximately 327 km offshore Rio de Janeiro, in water depths of 2238 m (Fig. 1(b)). The well intersected the Piçarras Formation, a lower syn-rift succession deposited during the Barremian stage. Lithological characterization was based on forty-four cutting samples (Table 1) collected at 3-m intervals between 6003 and 6029 m, plus one at 6031 m. To investigate the contact with the overlying Itapema Formation, analyses were also conducted on seventeen samples from its basal section, collected at 3-m intervals between 5952 and 6000 m.

Sampling depths were determined using the lag-time depth control methodology (Bourgoyne et al., 1986; Lapeyrouse, 2002; Mitchell et al., 2011). No continuous core samples were available for the Piçarras Formation, and only limited sidewall cores exist in some wells, which were not accessible for this study. Therefore, this research relied on cutting samples, which are widely available and provide continuous depth coverage for stratigraphic and mineralogical analyses. The Camboriu Formation, underlying the Piçarras, was not encountered in this well.

### 3.1. Geophysical well logs

Correlation between geochemical results, mineralogy, and geophysical well log responses was established using ten logs acquired through wireline (WL) and logging-while-drilling (LWD): gamma ray (GR), resistivity (RES), bulk density (RHOZ), neutron porosity (NPOR), photoelectric factor (PEF), compressional (DTCO) and shear sonic slowness (DTS), and magnetic resonance parameters, including free fluid ($NMR_{FF}$), capillarity ($NMR_{CAP}$), and clay-bound water ($NMR_{CWB}$). These logs were supported by caliper measurements (CAL). Due to differences in tool offsets in both LWD and WL configurations, logs were acquired over variable depth intervals (Table 2).

Wireline logs (WL) were depth-shifted using the LWD gamma ray (GR) curve as a reference, applying a shift factor (SF) calculated in Interactive Petrophysics® (IP). The method involves plotting the GR curves acquired from both LWD and WL measurements on the same scale and track and shifting the WL GR curve until it aligns with the LWD GR curve. The depth difference between the two curves defines the SF, which must subsequently be applied to all other WL log curves. This adjustment is essential whenever cutting samples are the focus of the study, as these samples, together with the LWD logs, are referenced to the drill bit depth. Although shifting the depth reference of WL logs is uncommon in the industry, this step was necessary for constructing the correlation framework.

To integrate well logs with mineralogical and geochemical data, log values were averaged over 3-m intervals corresponding to the cutting sample intervals. This approach yields a single representative value for each 3-m interval across all acquired geophysical logs. Although the vertical resolution of the logs provides approximately 19.68 measurements per 3-m interval, calculating a single representative value enables alignment of the well logs with the compositional mixing inherent in each cutting sample. This facilitates the application of statistical correlation methods.

### 3.2. Macroscopic and microscopic lithological description

A total of sixty-one cutting samples were analyzed under a Zeiss Stemi 508 Greenough stereo binocular stereomicroscope. Prior to analysis, 5 g of each sample were washed in five cycles alternating 99.8% pure isopropyl alcohol and deionized water to reduce olefin-based drilling mud contamination. Samples were analyzed in the wet state under the stereoscope. Lithological descriptions followed classifications from Dunham (1962), Folk (1968), Embry and Klovan (1971), Friedman et al. (1992), Demicco and Hardie (1994), Terra et al. (2010), Armelenti et al. (2016), Leite et al. (2020), and Tucker and Jones (2023). Quantification was qualitative, focusing on mineralogical composition, texture, and grain size. Detailed descriptions and images are provided in Supplementary S1 and S2.

### 3.3. Whole-sample X-ray diffractometry and fluorescence spectrometry

Whole-sample X-ray diffractometry (XRD) and fluorescence spectrometry (XRF) were performed on sixty-one cutting samples. XRD analyses were conducted at the Center for Mineral Technology (Brazil), and XRF analyses at COPEGEO, Fluminense Federal University (UFF). Each 25-g bulk sample was washed with liquid detergent and distilled water, dried at 60 °C for 24 h, milled to <106 μm using a planetary ball mill with tungsten carbide media, and dry-sieved.

Quantitative XRD analyses employed the Rietveld method (Rietveld, 1969; Cheary and Coelho, 1992) on a Bruker-AXS D8 Advance ECO diffractometer equipped with a LynxEye XE detector, operated at 40 kV and 25 mA using CuKα radiation ($\lambda = 1.54060$ Å).

**Table 1**
Summary of the described cutting samples and their corresponding laboratory analyses.

| Well | Stratigraphic unit | Analyzed interval, m | Sample cuttings described | Bulk sample analyses <106 μm | | Clay size analyses <2 μm | |
|---|---|---|---|---|---|---|---|
| | | | | XRF | XRD | XRF | XRD[a] |
| 1-BRSA-1363-RJS | Itapema Fm. | 5952/6000 | 17 | 17 | 17 | 17 | 68 |
| | Piçarras Fm. | 6000/6131 | 44 | 44 | 44 | 44 | 176 |

[a] These analyses comprise the combined results of glycolated, calcined, natural, and randomly oriented X-ray diffractograms.

**Table 2**
Logged depth interval summary of each logging tool, acquired via both wireline and logging while drilling methods.

| Mnemonic | Well log | Acquisition | Logged interval, m | | |
|---|---|---|---|---|---|
| | | | Top | Bottom | Total length |
| GR | Gamma-ray | LWD | 5950.0 | 6120.8 | 170.8 |
| RES | Resistivity (deep, medium and shallow) | LWD | 5950.0 | 6120.8 | 170.8 |
| DTCO | Sonic compressional | LWD | 5950.0 | 6091.3 | 141.3 |
| DTS | Sonic shear | LWD | 5950.0 | 6091.3 | 141.3 |
| GR | Gamma-ray | Wireline | 5950.0 | 6123.4 | 173.4 |
| $NMR_{FF}$ | Nuclear magnetic resonance (free fluid) | Wireline | 5950.0 | 6131.0 | 181.0 |
| $NMR_{CAP}$ | Nuclear magnetic resonance (capillarity fluid) | Wireline | 5950.0 | 6131.0 | 181.0 |
| $NMR_{CBW}$ | Nuclear magnetic resonance (clay bound water) | Wireline | 5950.0 | 6131.0 | 181.0 |
| NPOR | Neutrons | Wireline | 5950.0 | 6028.4 | 78.4 |
| RHOZ | Density | Wireline | 5950.0 | 6032.3 | 82.3 |
| PEF | Photoeletric factor | Wireline | 5950.0 | 6032.3 | 82.3 |
| CAL | Caliper | Wireline | 5950.0 | 6036.9 | 86.9 |

Data were collected over a range of 4°–90° $2\theta$ at 0.02°/s. Mineralogical quantification was performed using Bruker-AXS TOPAS v5 software and reference structures from the crystallographic open database (COD) and the ICDD PDF-4+ (Table 3). Mineral abbreviations follow Whitney and Evans (2010) and Warr (2021).

XRF analyses were performed using a Malvern Panalytical EPSILON 1 EDXRF spectrometer with an Ag anode, irradiating samples for 15 min in air for major and minor elements, and another 15 min for trace elements. Analyzed elements included major and minor oxides ($SiO_2$, $Al_2O_3$, $Fe_2O_3$, MnO, MgO, CaO, $K_2O$, $TiO_2$, $P_2O_5$) and trace elements (V, Cr, Co, Ni, Cu, Zn, Ga, As, Rb, Sr, Y, Zr, Nb, Ba, Ce, Pb, Th, U). Oxide contents were normalized to 100%, and trace elements reported in ppm, following Rollinson and Pease (2021). Calibration curves are provided in Supplementary S3 and S4. Siliciclastic mudstone and lime mudstone fragments were manually separated from cutting samples for targeted XRF and XRD analyses.

### 3.4. Qualitative clay mineral analyses

Sixty-one clay-sized aliquots were analyzed at COPEGEO/UFF. Ten grams were taken from each 25-g bulk sample for clay separation. Carbonates were removed using a buffered 4M solution of acetic acid (2M) and sodium acetate (2M), heated at 80 °C for 1 h (Carrado et al., 2006; Salgado-Campos et al., 2021; Coimbra et al., 2021). Decarbonation efficiency was confirmed by XRD. Organic matter was removed with hydrogen peroxide at 60 °C for 1 h. Clay fractions (<2 μm) were separated by centrifugation (Jackson, 1975; Whittig and Allardice, 1986; Moore and Reynolds, 1997).

Qualitative clay analyses were performed on random and oriented glass mounts, analyzed air-dried, glycolated (16 h), and after heating at 550 °C for 2 h, following Brindley and Brown (1980).

**Table 3**
Structures used in quantitative mineral analyses. COD – crystallographic open database; ICDD – international centre for diffraction data (PDF-4+).

| Structure | Code | Reference |
|---|---|---|
| Albite | ICDD 00-078-1995 | – |
| Barite | – | – |
| Calcite | – | Santos et al. (2017) |
| Dolomite | – | Santos et al. (2017) |
| Graphite | COD 1200018 | Lipson and Stokes (1942) |
| Halite | COD 9003309 | Walker et al. (2004) |
| Muscovite | ICDD 04-015-8226 | Brigatti et al. (2008) |
| Microcline | ICDD 00-019-0926 | Technisch Physiscge Dienst (1966) |
| Montmorillonite | COD 900277 | Viani et al. (2002) |
| Pyrite | ICDD 00-006-0710 | – |
| Quartz | ICDD 00-046-1045 | Kern and Eysel (1993) |

Diffraction patterns were obtained using a Bruker D2 Phaser diffractometer from 3° to 30° $2\theta$ (0.02°/s), except for random mounts scanned from 4° to 90° $2\theta$. The CuKα anode was operated at 300 W. Reflections at 1.54 Å in random mounts were compared to those at 1.82 Å to identify trioctahedral clays. Analyses were performed at LAMINX (UFF). Lithogeochemical analyses on clay fractions used the same EDXRF method described previously.

### 3.5. Statistical analysis and correlation framework

Statistical analyses were performed to investigate the relationships among mineralogical compositions, lithogeochemical data, and geophysical well log responses in both the Piçarras and Itapema formations. Initially, Shapiro–Wilk tests (Shapiro and Wilk, 1965) were applied to all geochemical datasets, including major, minor, and trace element concentrations (Supplementary S6), as well as to geophysical log measurements (Supplementary S7), to evaluate the normality of data distributions. The results indicated that most variables did not follow a normal distribution, justifying the application of non-parametric correlation techniques.

Consequently, Spearman rank correlation coefficients (Spearman, 1904) were calculated separately for the Piçarras and Itapema formations, considering the distinct mineralogical and geochemical characteristics of each unit. Correlation analyses encompassed mineral abundances obtained from whole-rock XRD, oxide contents and trace elements determined by XRF, and geophysical parameters from WL and LWD logs, including GR, RES, RHOZ, NPOR, PEF, DTCO and DTS, and nuclear magnetic resonance parameters ($NMR_{FF}$, $NMR_{CAP}$, $NMR_{CWB}$).

## 4. Results

### 4.1. Mineralogical characterization and clay mineral assemblages

A total of eleven minerals were identified through XRD analyses of cutting samples from well 1-BRSA-1363-RJS, including quartz, K-feldspar, plagioclase, mica (or illite), pyrite, calcite, dolomite, saponite, barite, halite, and gypsum (Figs. 2 and 3, Supplementary S10). Saponite and a fraction of the calcite are of authigenic origin, portions of quartz, mica, K-feldspar, and plagioclase are detrital, while other fractions of quartz, together with dolomite, pyrite, and part of the calcite, are diagenetic. Barite, halite, and gypsum are interpreted as contaminants derived from drilling fluids.

In well 1-BRSA-1363-RJS, the depth of 6000 m defines the contact between the Piçarras and Itapema formations, established as the first interval where saponite is entirely absent from cutting samples (Fig. 3). Saponite, a trioctahedral smectite, occurs

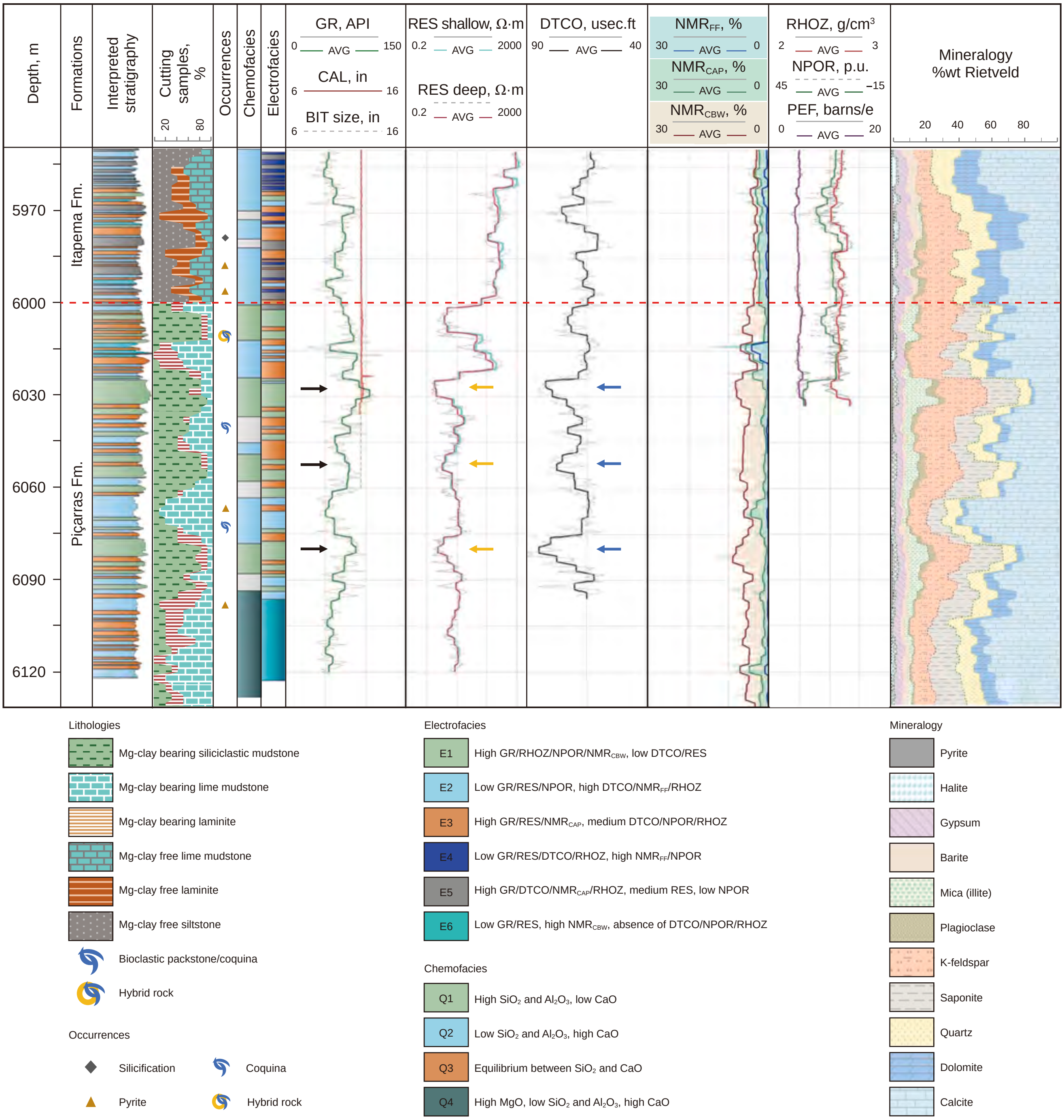


**Fig. 2.** Composite log for well 1-BRSA-1363-RJS, illustrating the alignment of well-log data with cutting sample intervals using a 3-m gridding methodology, enabling integrated analysis of petrophysical, mineralogical, and geochemical data. Depth-aligned logs include GR, RES, RHOZ, NPOR, PEF, DTCO, and nuclear magnetic resonance ($NMR_{FF}$, $NMR_{CAP}$, $NMR_{CBW}$). Six electrofacies were distinguished based on log variations. Elevated GR values (black arrows) indicate higher siliciclastic input, especially from K-feldspar, linked to chemofacies Q1 and electrofacies E1. Resistivity is lower in siliciclastic intervals (yellow arrows; Q1) and higher in carbonate-rich zones (Q2), while sonic slowness increases where mica is abundant (blue arrows). High $NMR_{CBW}$ correlates with clay-rich zones below 6000 m, marking the Piçarras Formation. The disappearance of saponite illustrates stratigraphic changes and highlights the lithological transition at 6000 m, defining the boundary between the Piçarras and Itapema formations (dashed red line) and aiding paleoenvironmental and diagenetic interpretations.

exclusively below this depth within the Piçarras Formation and is absent in shallower intervals, serving as a marker for the Mg-clay-free assemblage of the Itapema Formation. The mineral was characterized by diagnostic basal reflections under air-dried conditions at 14.12 Å, expanding to 16.46 Å after ethylene glycol solvation, contracting to 10 Å upon heating to 550 °C, and exhibiting a $d_{060}$ reflection at 1.535 Å (Fig. 4, Supplementary S5).

Saponite is associated with both siliciclastic and carbonate lithologies, but occurs in considerably higher volumes within siliciclastic rocks such as laminated siliciclastic mudstones. In intervals dominated by siliciclastics, saponite contents reach up to 22.0%, whereas in carbonate-rich samples, contents vary between 7.0% and 12.0%. Quantitative mineralogical data are presented in Table 4, with the complete dataset available in Supplementary S11.

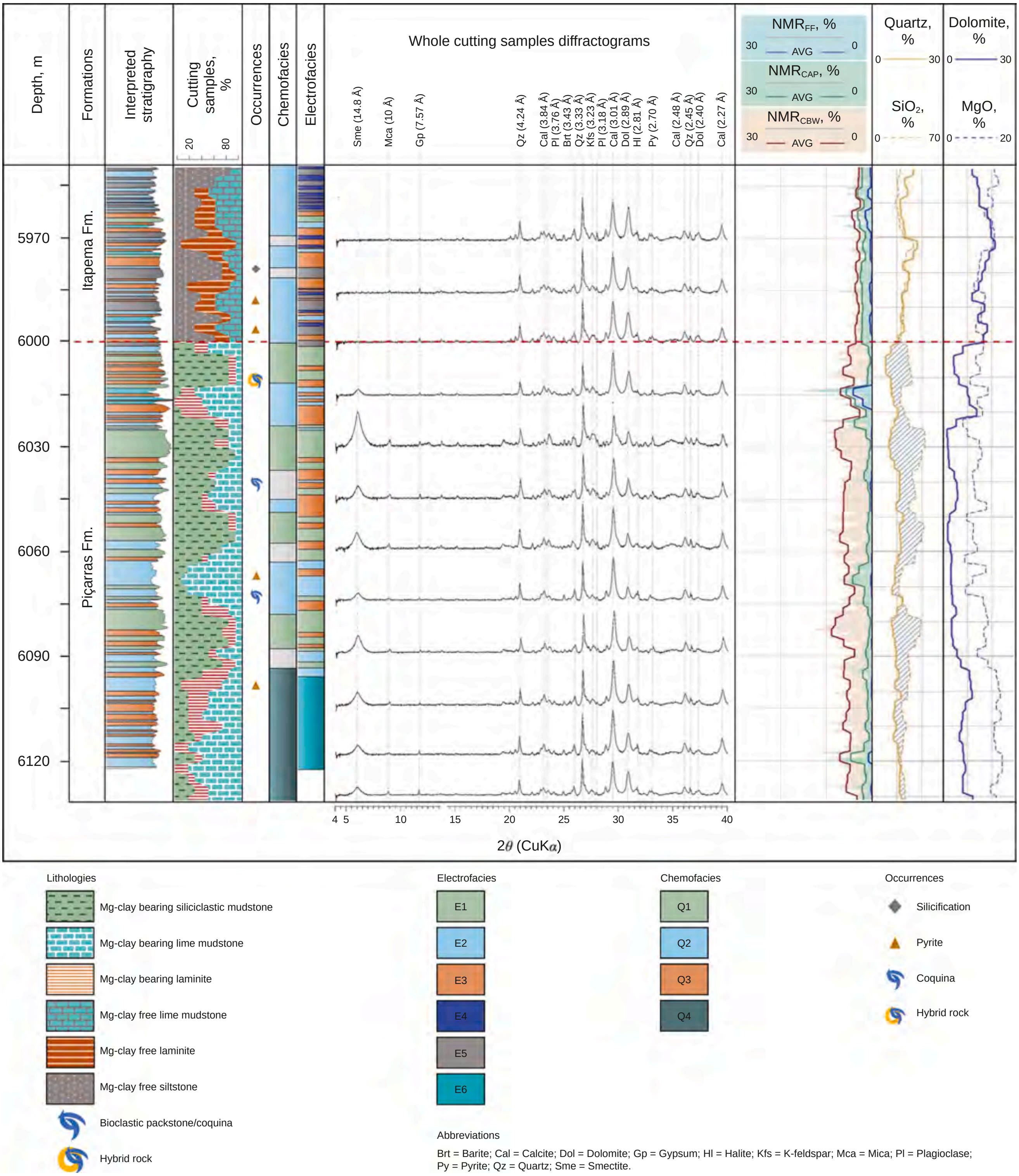


**Fig. 3.** Integration of mineralogical, lithogeochemical, and well-log data from well 1-BRSA-1363-RJS. The horizontal dashed line marks the abrupt contact between the Piçarras and Itapema formations at 6000 m. Above this depth, reflections associated with smectite disappear ($d_{001} = 14.8$ Å). This contact is also evident in the nuclear magnetic resonance log, where there is a significant increase in the volume of clay-bound water ($NMR_{CBW}$), associated with the higher contribution of saponite in the Piçarras Formation. Abrupt changes also occur in geochemical profiles, with a noticeable divergence between quartz (0–30%) and $SiO_2$ (0–70%), reflecting increased siliciclastic input in the Piçarras Formation. A separation between dolomite (0–30%) and MgO (0–20%) profiles suggests additional MgO contributions from saponite (smectite). Complete diffractograms are available in Supplementary S10.

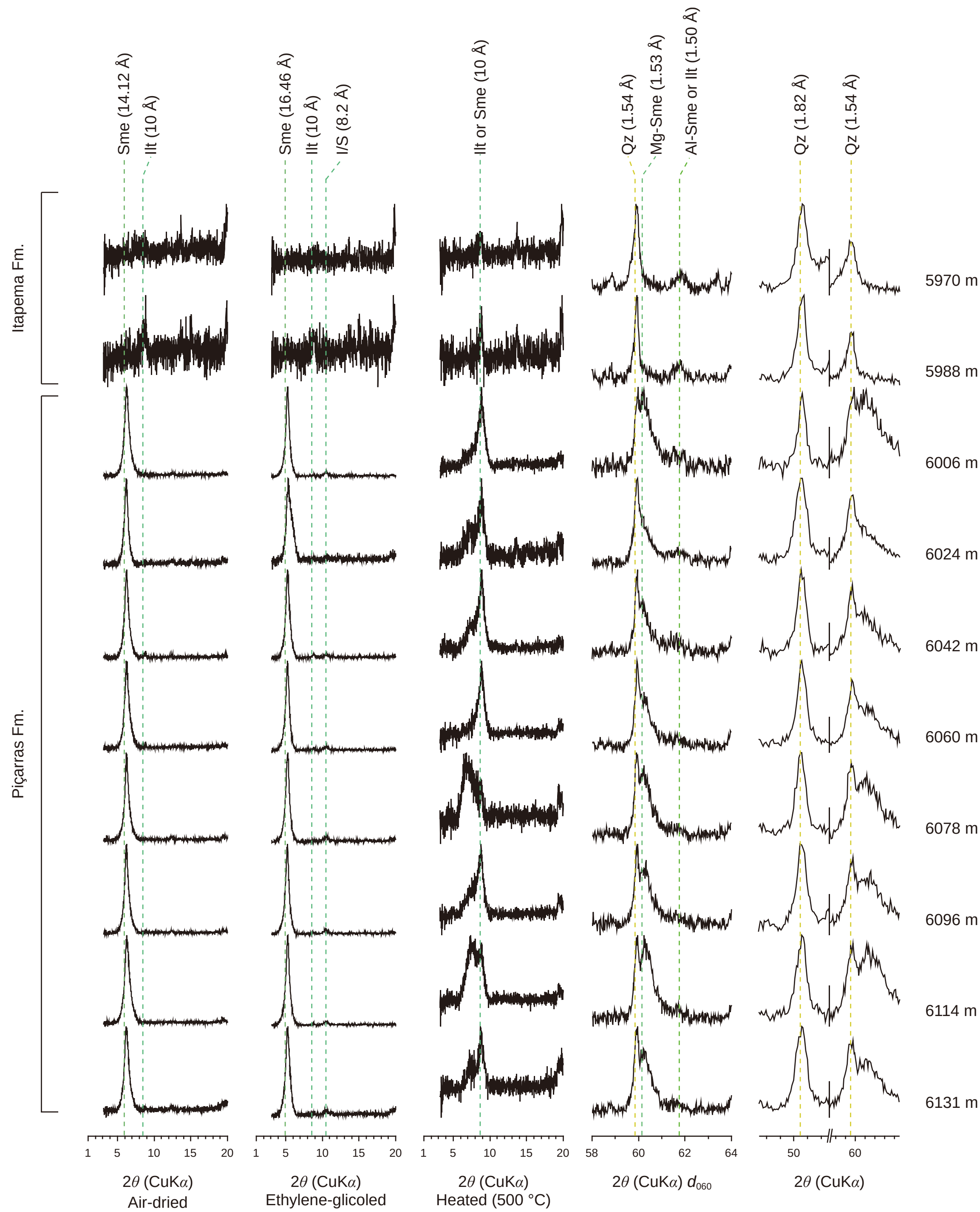


**Fig. 4.** Background-subtracted and normalized representative diffractograms of clay fractions from the Piçarras Formation. Saponite identified based on diagnostic reflections under air-dried conditions (14.12 Å), ethylene-glycol solvation (16.46 Å), and heating at 550 °C (10 Å), as well as its $d_{060}$ reflection (1.535 Å). Abbreviations: Sme – Smectite; Ilt – Illite; I/S – Interstratified Illite-Smectite; Qz – Quartz; Mg-Sme – Mg-smectite; Al-Sme – Al-smectite.

### *4.2. Lithogeochemistry and chemofacies analysis*

XRF analyses yielded data for nine major/minor and nineteen trace elements. For interpretative purposes, chemofacies were simplified based on variations in $Al_2O_3$, CaO, and MgO contents, resulting in four defined chemofacies (Q1 to Q4; Fig. 5). Lithogeochemical data for the Piçarras Formation are presented in Table 5, with complete datasets in Supplementary S12.

**Q1:** Characterized by increased $Al_2O_3$ (6.0%–9.2%), decreased CaO (39.0%–16.6%), and relatively low MgO (5.5%–12.2%), accompanied by elevated concentrations of $SiO_2$, $Fe_2O_3$, $K_2O$, $TiO_2$, $P_2O_5$, and various trace elements such as Cr, Co, Ni, Cu, Zn, Ga, Rb, Y, Zr, Nb, and Th.

**Q2:** Displays higher CaO (34.1%–60.0%) and lower $Al_2O_3$ (3.6%–5.6%), with MgO remaining relatively low. This chemofacies is associated with elevated Sr and U contents.

**Table 4**
Quantitative mineralogical data (%wt Rietveld) for whole samples of the Piçarras and Itapema formations from well 1-BRSA-1363-RJS, with each result representing a 9-m depth interval. Complete dataset (3-m) available in Supplementary S11. Abbreviations: Brt – barite; Cal – calcite; Dol – dolomite; Gp – gypsum; Hl – halite; Kfs – K-feldspar; Mca – mica; Pl – plagioclase; Py – pyrite; Qz – quartz; Sme – smectite.

| Depth, m | Cal, % | Kfs, % | Dol, % | Sme, % | Qz, % | Mca, % | Gp, % | Pl, % | Brt, % | Py, % | Hl, % |
|---|---|---|---|---|---|---|---|---|---|---|---|
| 5955 | 48.0 | 7.8 | 14.0 | 0.0 | 13.7 | 1.0 | 5.1 | 0.0 | 6.6 | 0.9 | 2.9 |
| 5964 | 42.5 | 12.5 | 18.0 | 0.0 | 11.8 | 1.4 | 5.7 | 0.0 | 6.1 | 1.6 | 0.4 |
| 5973 | 18.7 | 22.4 | 21.2 | 0.0 | 18.7 | 3.7 | 6.6 | 0.6 | 5.5 | 2.3 | 0.3 |
| 5982 | 21.2 | 26.1 | 15.9 | 0.0 | 15.3 | 2.8 | 6.7 | 6.3 | 3.6 | 1.8 | 0.3 |
| 5991 | 34.6 | 19.7 | 17.0 | 0.0 | 12.8 | 2.1 | 5.5 | 3.7 | 2.8 | 1.5 | 0.3 |
| 6000 | 36.0 | 21.7 | 16.3 | 0.0 | 10.8 | 1.2 | 5.4 | 1.7 | 4.5 | 1.5 | 0.9 |
| 6003 | 25.1 | 24.7 | 8.2 | 15.1 | 7.8 | 6.8 | 5.7 | 2.0 | 3.2 | 1.4 | 0.0 |
| 6012 | 26.3 | 26.2 | 6.7 | 14.6 | 7.7 | 9.1 | 4.7 | 2.1 | 0.6 | 2.0 | 0.0 |
| 6021 | 28.4 | 24.4 | 13.7 | 10.3 | 11.0 | 0.5 | 7.1 | 1.7 | 1.2 | 1.4 | 0.3 |
| 6030 | 14.6 | 29.8 | 2.1 | 19.3 | 7.1 | 14.5 | 3.4 | 5.7 | 1.6 | 1.9 | 0.0 |
| 6039 | 34.6 | 20.9 | 4.8 | 12.0 | 11.3 | 4.4 | 5.3 | 3.5 | 1.6 | 1.6 | 0.0 |
| 6048 | 39.6 | 19.9 | 5.4 | 10.6 | 9.9 | 5.0 | 5.4 | 1.1 | 2.0 | 1.1 | 0.0 |
| 6057 | 25.6 | 22.1 | 2.1 | 17.4 | 11.8 | 10.6 | 3.4 | 4.1 | 1.6 | 1.3 | 0.0 |
| 6066 | 55.4 | 12.9 | 3.3 | 7.7 | 9.5 | 3.8 | 2.9 | 0.8 | 2.1 | 1.1 | 0.5 |
| 6075 | 47.6 | 10.8 | 3.9 | 12.3 | 12.5 | 2.8 | 2.7 | 1.2 | 4.8 | 0.7 | 0.7 |
| 6084 | 21.4 | 19.0 | 3.7 | 20.0 | 8.7 | 13.6 | 4.3 | 4.4 | 2.7 | 1.7 | 0.5 |
| 6093 | 35.7 | 18.7 | 7.3 | 7.8 | 9.9 | 8.0 | 6.0 | 1.1 | 3.1 | 1.8 | 0.6 |
| 6102 | 28.2 | 12.7 | 12.0 | 20.1 | 12.0 | 3.8 | 4.1 | 1.4 | 3.5 | 1.3 | 0.9 |
| 6111 | 40.8 | 10.4 | 7.6 | 17.0 | 10.2 | 5.1 | 3.6 | 1.2 | 2.6 | 0.9 | 0.6 |
| 6120 | 42.2 | 9.4 | 8.5 | 16.2 | 11.0 | 2.8 | 3.5 | 1.0 | 3.7 | 0.7 | 1.0 |
| 6129 | 36.6 | 12.7 | 8.2 | 16.9 | 11.4 | 3.4 | 4.2 | 1.0 | 3.6 | 1.2 | 0.8 |
| 6131 | 30.7 | 11.4 | 12.5 | 19.0 | 12.1 | 2.6 | 4.2 | 2.2 | 3.9 | 1.2 | 0.6 |

**Q3:** Exhibits balanced proportions of CaO and $Al_2O_3$, while other elements remain at moderate levels.

**Q4:** Defined by the highest MgO values (12.9%–16.1%), with CaO (40.4%–48.5%) predominating over $Al_2O_3$ (4.1%–5.2%).

### *4.3. Well logs description and electrofacies classification*

Six electrofacies were identified based on variations in petrophysical log responses (Fig. 2):

**E1:** Exhibits high gamma ray readings (69–113 gAPI), low resistivity (1.3–5.8 Ω·m), elevated compressional slowness (91–76 μs/ft), high density (2.45–2.53 g/cm$^3$), elevated neutron porosity (28.4–17.3 p.u.), high clay-bound water content (12.7 p.u.), minimal free fluid, and photoelectric factor (PEF) values between 4.4 and 4.8 b/electron.

**E2:** Characterized by low gamma ray values (27–51 gAPI), corresponding to Mg-clay-bearing laminated lime mudstones and Mg-clay-free laminated lime mudstones, moderate resistivity (12.5–13.4 Ω·m), lower compressional slowness (62–64 μs/ft), overlapping density (2.56–2.64 g/cm$^3$) and neutron porosity (10.6–17.9 p.u.), high free fluid (11.9–4.9 p.u.), and low clay-bound water. PEF averages approximately 5.3 b/electron.

**E3:** Represents intermediate responses between E1 and E2, with gamma ray readings of 60–80 gAPI, resistivity of 5.0–15.0 Ω·m, compressional slowness between 60 and 70 μs/ft, density of 2.50–2.70 g/cm$^3$, neutron porosity of 9.0–15.0 p.u., and relatively high capillarity (3.0 p.u.). PEF ranges from 4.0 to 5.0 b/electron.

**E4:** Displays low gamma ray values (44–53 gAPI), higher resistivity (11.9–20.0 Ω·m), low compressional slowness (62–64 μs/ft), density of 2.48 g/cm$^3$, neutron porosity of 12.0 p.u., high capillarity (3.5–4.9 p.u.), low free fluid (0.3 p.u.), and PEF around 4.6 b/electron.

**E5:** Exhibits high gamma ray responses (70–94 gAPI), significant resistivity (100.0–1200.0 Ω·m), low compressional slowness (57–62 μs/ft), density of 2.58–2.68 g/cm$^3$, low neutron porosity (0.6–1.3 p.u.), high capillarity (2.1–3.4 p.u.), and PEF near 4.6 b/electron.

**E6:** Lacks DTCO, DTS, RHOZ, NPOR, and PEF logs due to offset limitations, with gamma ray values of 39–75 gAPI, moderate resistivity (3.3–11.2 Ω·m), and clay-bound water predominating over capillarity and free fluid.

### *4.4. Macroscopic and microscopic lithofacies description*

Eight lithologies were recognized and classified into two principal lithofacies assemblages: Mg-clay-bearing (Fig. 6) and Mg-clay-free units (Fig. 7). This division is significant, as the presence of Mg-clay minerals is exclusive to the Piçarras Formation and entirely absent in the overlying Itapema Formation, thereby providing a key mineralogical criterion for differentiating between these stratigraphic units. These assemblages are delineated by abrupt transitions corresponding to distinct mineralogical and geophysical signatures. Eleven rock fragments from the Mg-clay-bearing assemblage were further analyzed through thin-section petrography. Additionally, XRF (Table 6) and XRD (Table 7) analyses were performed on selected samples of siliciclastic mudstone and lime mudstone.

#### *4.4.1. Mg-clay-bearing lithologies*

*4.4.1.1. Laminites.* The Mg-clay-bearing laminites (Fig. 6(a)–(c)) display wavy rhythmic lamination formed by discontinuous carbonate and Mg-clay-rich siliciclastic couplets, with laminae typically measuring 50–100 μm in thickness. They are light to medium brown in color and occur exclusively within the Piçarras Formation, representing about 30% of its rock volume.

XRD analyses of whole cutting samples from intervals rich in laminites indicate a mineral assemblage consisting of saponite (15.0%–20.0%), K-feldspar (12.0%–18.0%), quartz (10.0%), mica (3.0%–5.0%), and plagioclase (1.5%–2.5%) in the siliciclastic layers, while calcite (25.0%–30.0%) and dolomite (10.0%–12.0%) dominate the carbonate layers. Mineral proportions vary between samples due to lithological differences and diagenetic effects.

Thin-section petrography (Fig. 6(c)) reveals the siliciclastic couplets to comprise angular to subrounded grains of orthoclase, quartz, and muscovite, with minor biotite, labradorite, opaque minerals, and clays. Orthoclase, biotite, and muscovite often show

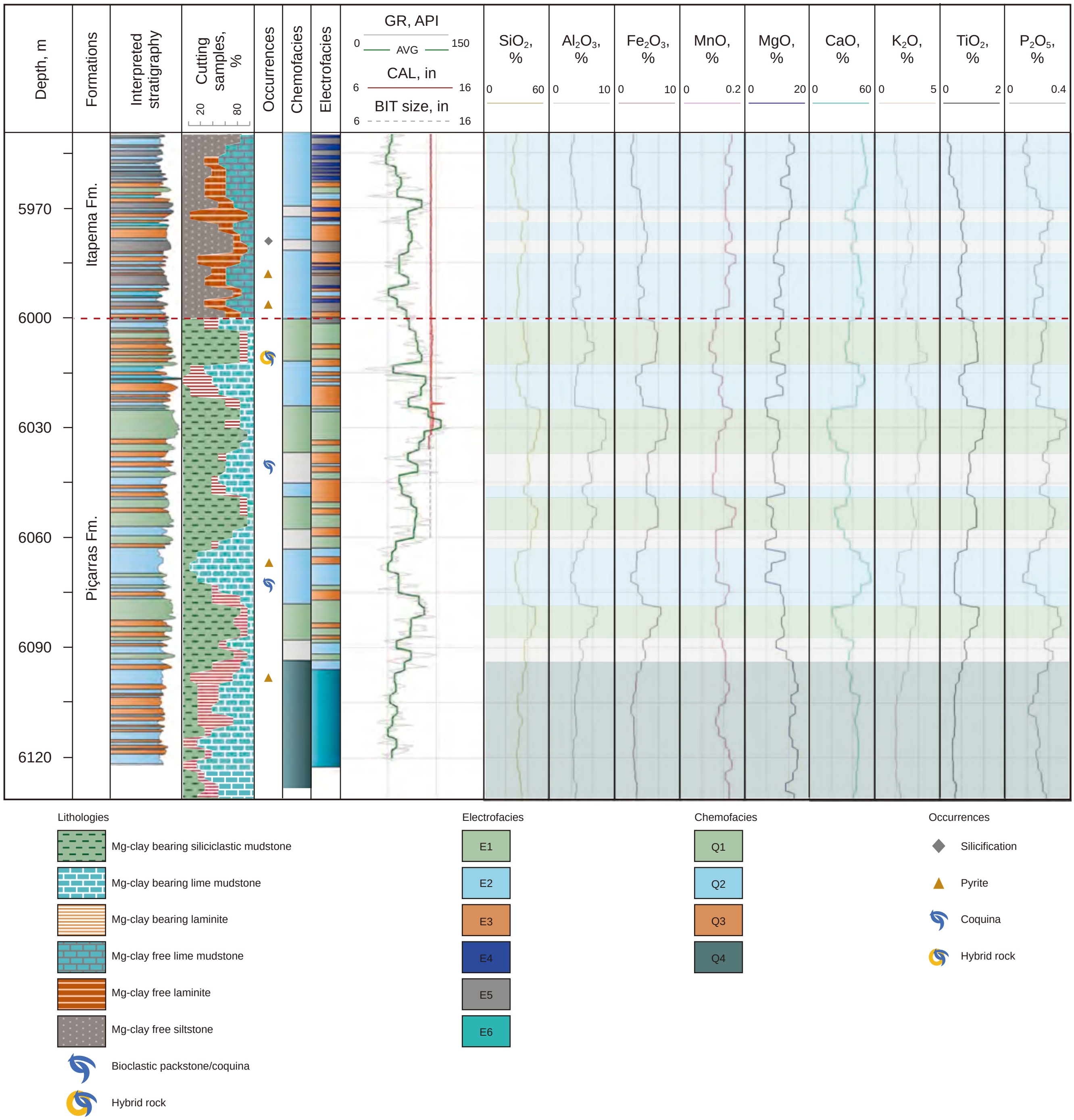


**Fig. 5.** Boundaries of distinct lithogeochemical signatures defining four chemofacies (Q1, Q2, Q3, and Q4), based on variations of three oxide indices: $Al_2O_3$, CaO, and MgO.

partial dissolution, while saponite forms discontinuous, crenulated layers surrounding detrital grains. Opaque minerals, including pyrite, tend to concentrate along saponite-rich laminae.

In the carbonate-rich couplets, calcite occurs as microcrystalline aggregates or silt-sized grains with sutured contacts and diffuse edges. Dolomite displays a more euhedral to subhedral habit and well-defined grain boundaries, often appearing as discrete crystals or as cement within the carbonate matrix.

*4.4.1.2. Laminated siliciclastic mudstone.* The Mg-clay-bearing laminated siliciclastic mudstone is distinguished by an olive-green to greenish-brown coloration and displays very fine plane-parallel lamination (Fig. 6(d)–(f)). Dispersed silt-sized grains are typically concentrated within darker laminae, and the relative proportions of silt and clay vary across the drilled interval. This lithology represents approximately 31% of the Piçarras Formation.

The mineral assemblage comprises saponite (39.4%), K-feldspar (24.0%), mica (6.2%), plagioclase (3.8%), calcite (11.0%), quartz (9.5%), pyrite (2.6%), and dolomite (1.0%), with traces of barite (<1%), gypsum (1.0%), and halite (1.5%), the latter likely related to drilling fluids. Mineral proportions vary due to lithological distribution and diagenetic alteration.

**Table 5**
Lithogeochemical analysis of Piçarras Formation samples using the XRF method, with each result representing a 12-m depth interval. Depth references correspond to the bottom of each 12-m interval. Complete dataset (3-m) including lithogeochemistry results for the Itapema Formation can be found in Supplementary S12.

| Depth, m | 6003 | 6015 | 6027 | 6039 | 6051 | 6063 | 6075 | 6087 | 6099 | 6111 | 6123 | 6131 |
|---|---|---|---|---|---|---|---|---|---|---|---|---|
| $SiO_2$, % | 33.13 | 26.80 | 49.56 | 37.50 | 40.83 | 40.11 | 28.53 | 40.91 | 33.31 | 31.86 | 27.63 | 31.34 |
| $Al_2O_3$, % | 6.09 | 4.85 | 8.30 | 6.57 | 6.49 | 5.90 | 4.49 | 6.45 | 4.96 | 4.59 | 4.16 | 4.53 |
| $Fe_2O_3$, % | 5.95 | 4.02 | 7.89 | 4.97 | 6.25 | 4.57 | 3.46 | 5.32 | 3.18 | 2.82 | 2.86 | 3.20 |
| MnO, % | 0.11 | 0.11 | 0.16 | 0.12 | 0.15 | 0.12 | 0.16 | 0.12 | 0.15 | 0.12 | 0.17 | 0.16 |
| MgO, % | 11.00 | 12.23 | 6.80 | 8.14 | 6.48 | 5.96 | 11.00 | 11.70 | 15.01 | 13.96 | 16.12 | 14.54 |
| CaO, % | 38.89 | 48.25 | 21.11 | 37.91 | 35.45 | 39.36 | 49.79 | 31.41 | 40.40 | 44.43 | 46.85 | 43.51 |
| $K_2O$, % | 3.44 | 2.73 | 4.25 | 3.57 | 2.90 | 2.87 | 1.91 | 2.83 | 2.18 | 1.55 | 1.59 | 2.01 |
| $TiO_2$, % | 1.12 | 0.80 | 1.64 | 0.96 | 1.19 | 0.86 | 0.43 | 0.98 | 0.60 | 0.45 | 0.39 | 0.45 |
| $P_2O_5$, % | 0.26 | 0.21 | 0.29 | 0.25 | 0.26 | 0.25 | 0.23 | 0.28 | 0.22 | 0.22 | 0.23 | 0.27 |
| V, ppm | 163 | 87 | 168 | 127 | 157 | 93 | 152 | 190 | 98 | 129 | 129 | 153 |
| Cr, ppm | 0 | 20 | 76 | 10 | 5 | 27 | 0 | 0 | 10 | 0 | 0 | 0 |
| Co, ppm | 10 | 6 | 15 | 8 | 10 | 7 | 5 | 10 | 6 | 5 | 4 | 5 |
| Ni, ppm | 54 | 31 | 87 | 38 | 55 | 36 | 21 | 58 | 27 | 18 | 17 | 25 |
| Cu, ppm | 42 | 24 | 51 | 34 | 50 | 29 | 28 | 42 | 26 | 26 | 26 | 34 |
| Zn, ppm | 96 | 40 | 73 | 58 | 60 | 49 | 76 | 96 | 61 | 64 | 72 | 101 |
| Ga, ppm | 4 | 3 | 6 | 5 | 3 | 4 | 1 | 4 | 2 | 3 | 2 | 3 |
| As, ppm | 9 | 10 | 8 | 11 | 9 | 11 | 9 | 12 | 14 | 11 | 10 | 12 |
| Rb, ppm | 29 | 27 | 36 | 34 | 28 | 29 | 18 | 34 | 26 | 20 | 16 | 21 |
| Sr, ppm | 1533 | 1364 | 588 | 1095 | 1133 | 1041 | 1639 | 1174 | 1153 | 1394 | 1321 | 1261 |
| Y, ppm | 9 | 8 | 13 | 10 | 9 | 8 | 5 | 10 | 7 | 5 | 4 | 6 |
| Zr, ppm | 105 | 86 | 152 | 119 | 112 | 94 | 56 | 119 | 78 | 58 | 56 | 67 |
| Nb, ppm | 8 | 5 | 13 | 7 | 9 | 6 | 3 | 9 | 5 | 4 | 4 | 4 |
| Ba, ppm | 15500 | 3968 | 3035 | 7441 | 10364 | 2667 | 20320 | 14988 | 3904 | 12805 | 16010 | 19031 |
| Ce, ppm | 42.5 | 34.1 | 54.7 | 42.6 | 50.5 | 33.8 | 60.9 | 46.0 | 30.1 | 31.7 | 46.0 | 47.0 |
| Pb, ppm | 11 | 4 | 9 | 6 | 11 | 3 | 16 | 10 | 7 | 6 | 14 | 12 |
| Th, ppm | 0.0 | 0.0 | 1.4 | 0.1 | 0.3 | 0.0 | 0.0 | 0.0 | 0.0 | 0.0 | 0.0 | 0.0 |
| U, ppm | 4.7 | 5.6 | 2.0 | 4.4 | 3.8 | 4.2 | 5.8 | 4.4 | 4.4 | 5.3 | 4.7 | 4.2 |

Thin-section observations reveal a matrix dominated by saponite, orthoclase, muscovite, quartz, and minor labradorite and opaques. Saponite appears both as thin laminae and as a diffuse matrix component, while pyrite is distributed homogeneously, often aligned with saponite-rich layers. Organic matter is present as rounded to elongate clasts ranging from 30 to 100 μm.

*4.4.1.3. Lime mudstone.* The Mg-clay-bearing lime mudstone is light grey to white and predominantly massive in texture, though weak to well-developed plane-parallel laminations occur locally (Fig. 6(g)–(i)). Carbonate laminations are interbedded with thin, discontinuous, crenulated layers of saponite. Organic matter occurs as grains smaller than 50 μm, and dolomite appears as anhedral crystals less than 100 μm in size.

XRD analyses reveal a mineral assemblage dominated by calcite (23.0%–57.0%), typically as micrite, with orthoclase (10.0%–13.0%), saponite (8.0%–11.0%), quartz (8.0%–9.0%), dolomite (3.5%), mica (1.0%–3.0%), and minor plagioclase (<1%). Variations reflect both stratigraphic position and diagenetic influence. This lithology accounts for 36.0% of the Piçarras Formation. Thin-section analysis confirms calcite mainly as micrite but also as microcrystalline aggregates, with sparse opaque minerals occurring locally.

*4.4.1.4. Fragmented bioclastic packstone (coquina).* The Mg-clay-bearing fragmented bioclastic packstone (coquina) appears white to grey and occasionally exhibits a vitreous translucent aspect. It comprises fragmented bioclasts smaller than 300 μm, frequently showing loss of shell morphology due to compaction (Fig. 6(j)). Coquinas are notably associated with levels rich in organic matter. Saponite is present as dispersed, unoriented fine-sand to silt-sized rounded grains.

The mineralogical composition includes calcite (57.0%), K-feldspar (10.0%), saponite (9.0%), quartz (8.0%), dolomite (4.0%), mica (2.0%), and plagioclase (<1%). Coquina is difficult to identify in cutting samples due to its small, fragmented nature, often obscured by micrite, preventing reliable quantification of its overall abundance. This lithofacies occurs in several submetric beds within the drilled interval but is linked to saponite only below 6000 m. It constitutes approximately 3.0% of the Piçarras Formation.

Under macroscopic examination of drilling cuttings, distinguishing purely bioclastic rocks from hybrid mixtures involving siliciclastic grains, magnesium clay minerals, and bioclastic fragments remains challenging. However, coquina occurrences correlate with low gamma ray readings and low porosity, while hybrid rocks display higher gamma ray values and elevated porosity due to Mg-clay content.

*4.4.1.5. Hybrid rock.* Hybrid rocks (Fig. 6(k) and (l)) consist of a massive mixture of fine-to medium-grained saponite peloids and fragmented bioclasts, likely derived from bivalves. They display a light brown to yellowish color. Thin-section observations indicate lower amounts of opaque minerals, while subhedral dolomite and anhedral calcite act as cement or replacement phases within the bioclastic matrix. Saponite occurs as well-rounded peloids, often exhibiting diagenetic transformations into dolomite.

### *4.4.2. Mg-clay-free lithologies*

*4.4.2.1. Laminites.* Mg-clay-free laminites exhibit light to medium brown coloration and wavy rhythmic lamination, forming discontinuous carbonate-siliciclastic couplets that incorporate organic matter and measure between 30 and 80 μm in thickness (Fig. 7(a)). These laminites are confined to the Itapema Formation, occurring exclusively above 6000 m, and are interbedded with other lithologies.

The mineralogical composition of the siliciclastic-dominated layers includes K-feldspar (22.5%), quartz (18.0%), mica (3.0%), and plagioclase (<1.0%), while the carbonate-dominated layers comprise calcite (35.0%) and dolomite (21.0%). Lithological and diagenetic variations influence mineral proportions. Laminites constitute approximately 26.0% of the Itapema Formation.

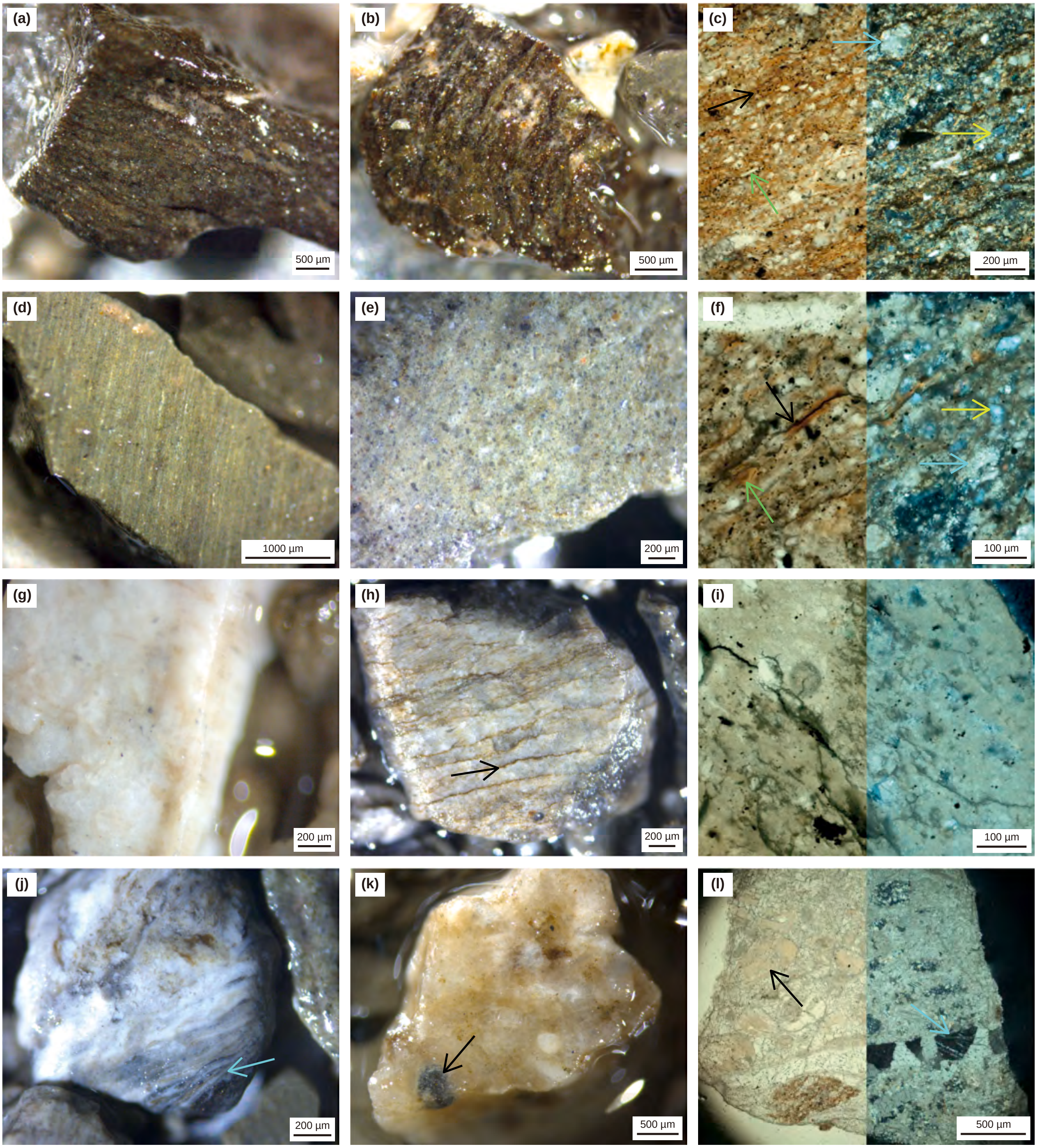


**Fig. 6.** Types of Mg-clay-bearing lithologies: (**a**) Mg-clay-bearing laminite; (**b**) discontinuous carbonate-siliciclastic couplets with wavy rhythmic lamination; (**c**) photomicrograph* of representative laminite lithology showing primary constituents: calcite (blue arrow), quartz and orthoclase (yellow arrow), muscovite (green arrow), and saponite (black arrow); (**d**) Mg-clay-bearing very fine laminated siliciclastic mudstone; (**e**) dispersed silt-sized grains; (**f**) photomicrograph* of representative siliciclastic mudstone lithology showing primary constituents as in (**c**); (**g**) Mg-clay-bearing lime mudstone, massive to (**h**) well-developed plane-parallel lamination intercalated with saponite layers (black arrow); (**i**) photomicrograph* of representative lime mudstone lithology showing micrite and opaque minerals; (**j**) Mg-clay-bearing fragmented bioclastic packstone (coquina); (**k**) hybrid bioclastic "stevensitic" arenite showing medium-grained saponite peloids; (**l**) photomicrograph* of representative hybrid rock showing medium-grained saponite peloids (black arrow) and recrystallized bioclast (probably bivalve–blue arrow) in a dolomitized matrix.
*Photomicrographs (**c**), (**f**), (**i**), and (**l**): left side in plane-polarized light and right side in crossed polarized light.

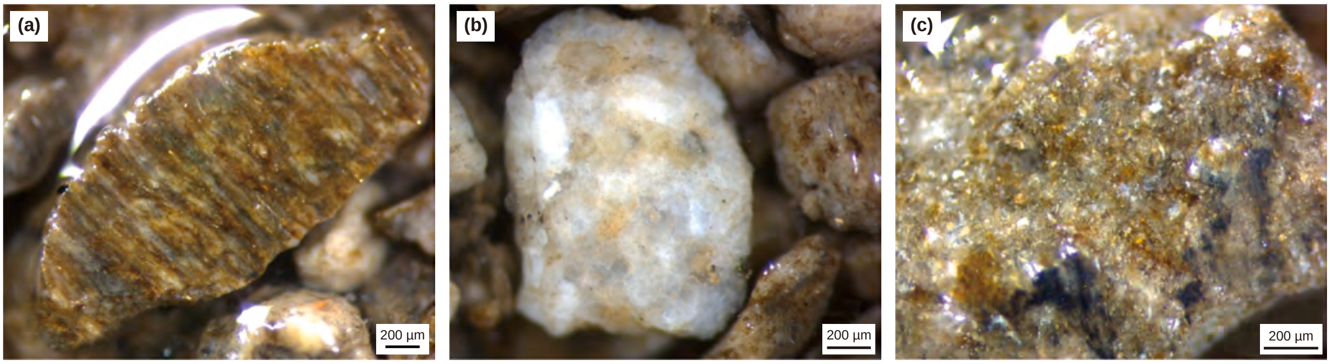


**Fig. 7.** Types of Mg-clay-free lithologies: (**a**) Mg-clay-free laminite with wavy rhythmic lamination, consisting of discontinuous carbonate-siliciclastic couplets associated with organic matter; (**b**) Mg-clay-free lime mudstone, predominantly massive; (**c**) Mg-clay-free weakly laminated siltstone.

**Table 6**
XRF analyses performed on selected samples of siliciclastic mudstone and lime mudstone.

| Chemical elements | Unit | Siliciclastic mudstone | Lime mudstone |
|---|---|---|---|
| $SiO_2$ | % | 52.68 | 20.39 |
| $Al_2O_3$ | % | 10.41 | 3.67 |
| $Fe_2O_3$ | % | 8.44 | 2.10 |
| MnO | % | 0.07 | 0.13 |
| MgO | % | 11.72 | 6.93 |
| CaO | % | 9.59 | 65.34 |
| $K_2O$ | % | 4.84 | 1.13 |
| $TiO_2$ | % | 1.90 | 0.34 |
| $P_2O_5$ | % | 0.35 | 0.00 |
| V | ppm | 221 | 46 |
| Cr | ppm | 129 | 0 |
| Co | ppm | 22 | 2 |
| Ni | ppm | 205 | 19 |
| Cu | ppm | 61 | 14 |
| Zn | ppm | 113 | 32 |
| Ga | ppm | 9 | 2 |
| As | ppm | 9 | 5 |
| Rb | ppm | 60 | 11 |
| Sr | ppm | 441 | 1468 |
| Y | ppm | 19 | 4 |
| Zr | ppm | 241 | 49 |
| Nb | ppm | 31 | 1 |
| Ba | ppm | 2905 | 4029 |
| Ce | ppm | 48.7 | 0.0 |
| Pb | ppm | 16 | 4 |
| Th | ppm | 1.2 | 0.4 |
| U | ppm | 1.1 | 8.5 |

**Table 7**
XRD analyses performed on selected samples of siliciclastic mudstone and lime mudstone.

| Mineralogy | Unit | Siliciclastic mudstone | Lime mudstone |
|---|---|---|---|
| Calcite | %wt Rietveld | 11.00 | 74.30 |
| Dolomite | %wt Rietveld | 1.00 | 3.90 |
| Saponite | %wt Rietveld | 39.40 | 8.00 |
| K-feldspar | %wt Rietveld | 24.00 | 2.00 |
| Quartz | %wt Rietveld | 9.50 | 9.80 |
| Plagioclase | %wt Rietveld | 3.80 | 1.00 |
| Pyrite | %wt Rietveld | 2.60 | 1.00 |
| Mica | %wt Rietveld | 6.20 | – |
| Halite | %wt Rietveld | 1.50 | – |
| Gypsum | %wt Rietveld | 1.00 | – |

*4.4.2.2. Lime mudstone.* Mg-clay-free lime mudstone is characterized by a light grey to white color and predominantly massive texture, although weak plane-parallel lamination is occasionally observed (Fig. 7(b)). Organic matter is dispersed as approximately 50 μm spots, while anhedral dolomite occurs as grains smaller than 100 μm.

The mineralogy comprises calcite (46.0%–48.0%), quartz (13.0%–17.0%), dolomite (12.0%–15.0%), and K-feldspar (7.0%–10.0%). Mineral proportions vary due to stratigraphic position and diagenetic processes. This lithofacies occurs exclusively in the Itapema Formation above 6000 m, constituting around 26.0% of the total rock volume.

*4.4.2.3. Weak-laminated siltstone.* The Mg-clay-free weak-laminated siltstone (Fig. 7(c)) ranges in color from light to orangish grey and displays weak plane-parallel lamination. It is composed predominantly of silt-sized grains, including K-feldspar (20.0%–25.0%), calcite (18.0%–25.0%), dolomite (17.0%–21.8%), quartz (12.0%–18.0%), plagioclase (<3.0%), and mica (<3.0%). Organic matter occurs as fine, dispersed spots. This lithology is exclusive to the Itapema Formation and accounts for approximately 38.0% of its rock volume. The proportions of these minerals vary among samples, reflecting differences in depositional settings and diagenetic influence.

*4.4.3. Diagenetic products*

Stereomicroscopic observations revealed a suite of diagenetic minerals, notably dolomite, pyrite, calcite, saponite, and quartz (Fig. 8). Quantification of these phases was performed using the Rietveld method applied to XRD bulk mineralogy data (Supplementary S11).

Dolomite, the most abundant diagenetic constituent in carbonate lithologies, primarily exhibits a macrocrystalline, often anhedral habit, with subordinate microcrystalline forms. The highest dolomite contents were recorded above 6,021 m (maximum 21.2%, average 14.7%) and below 6090 m (maximum 12.1%, average 9.1%), showing strong association with laminites (Spearman correlation = 0.73 in the Piçarras Formation). Dolomite infills vuggy porosity in lime mudstones (Fig. 8(a)) and, in some intervals, pervasive dolomitization completely (Fig. 8(b)) or partially (Fig. 8(c)) obliterates original rock textures. Thin-section observations indicate replacement of saponite by dolomite in hybrid rocks (Fig. 9(c)).

Calcite occurs in three morphologies: crypto-to fine-crystalline (Fig. 9(b)–(d)), macrocrystalline (Figs. 8(d) and 9(a)), and blocky textures (Fig. 9(a), (d) and (f)).

Pyrite predominantly forms in siliciclastic mudstones, appearing as microcrystalline disseminations, often occupying fracture

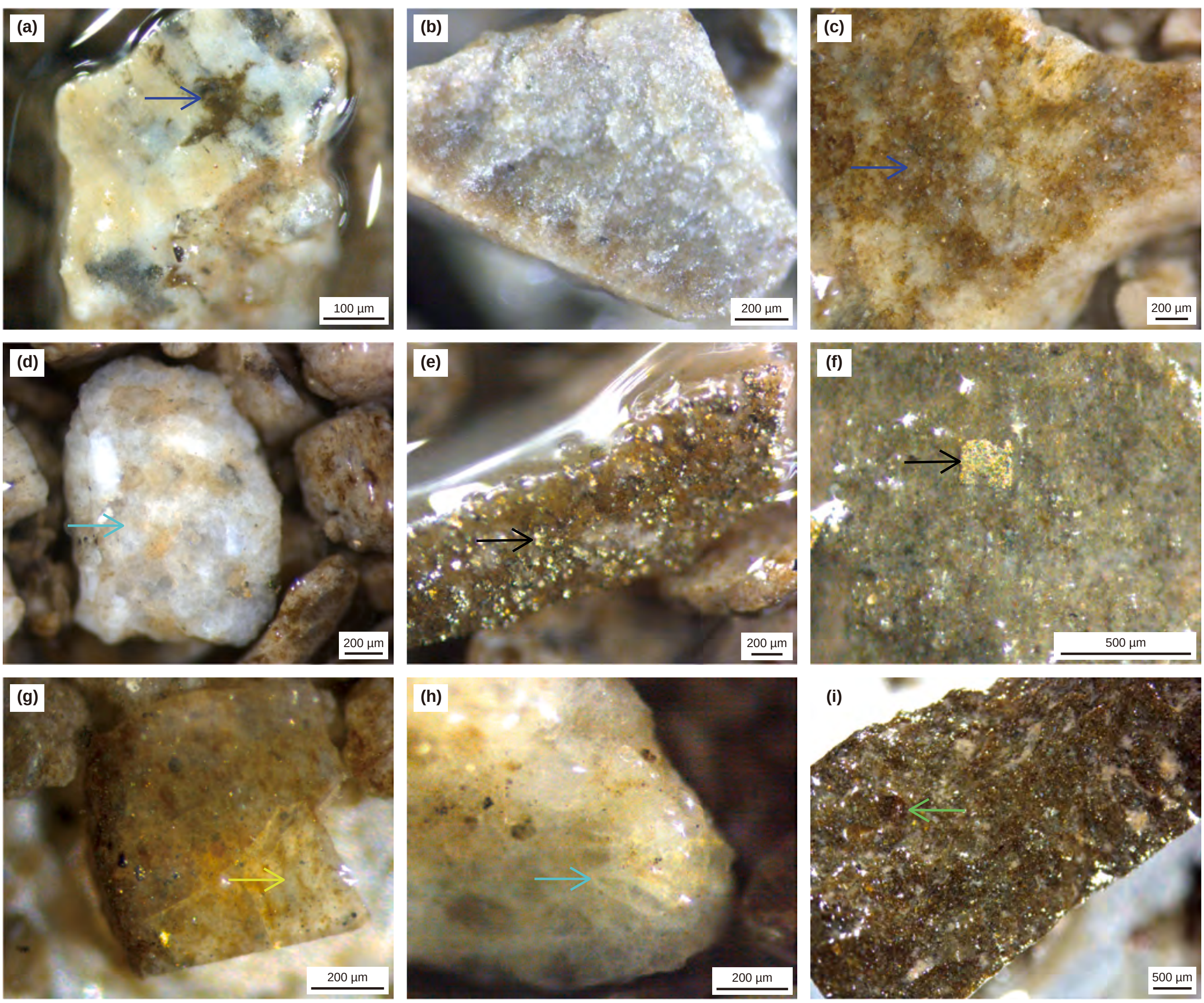


**Fig. 8.** Common diagenetic features observed under stereomicroscope analysis. (**a**) Blocky dolomite (blue arrow) probably filling vuggy pore space in lime mudstone; (**b**) sucrosic dolostone indicating pervasive dolomitization that totally (b) or partially (**c**, blue arrow) obliterates the rock fabric; (**d**) macrocrystalline calcite; (**e**) microcrystalline disseminated pyrite (black arrow) probably filling fractures; (**f**) cubic euhedral pyrite (black arrow) in siliciclastic mudstone; (**g**) pervasive silicification (yellow arrow) in lime mudstone, completely obliterating the rock fabric; (**h**) bioclastic grainstone (coquina) cemented by displacive silica (light blue arrow); (**i**) granular (green arrow) and laminated saponite formed from the alteration of precursor minerals such as mica and feldspar.

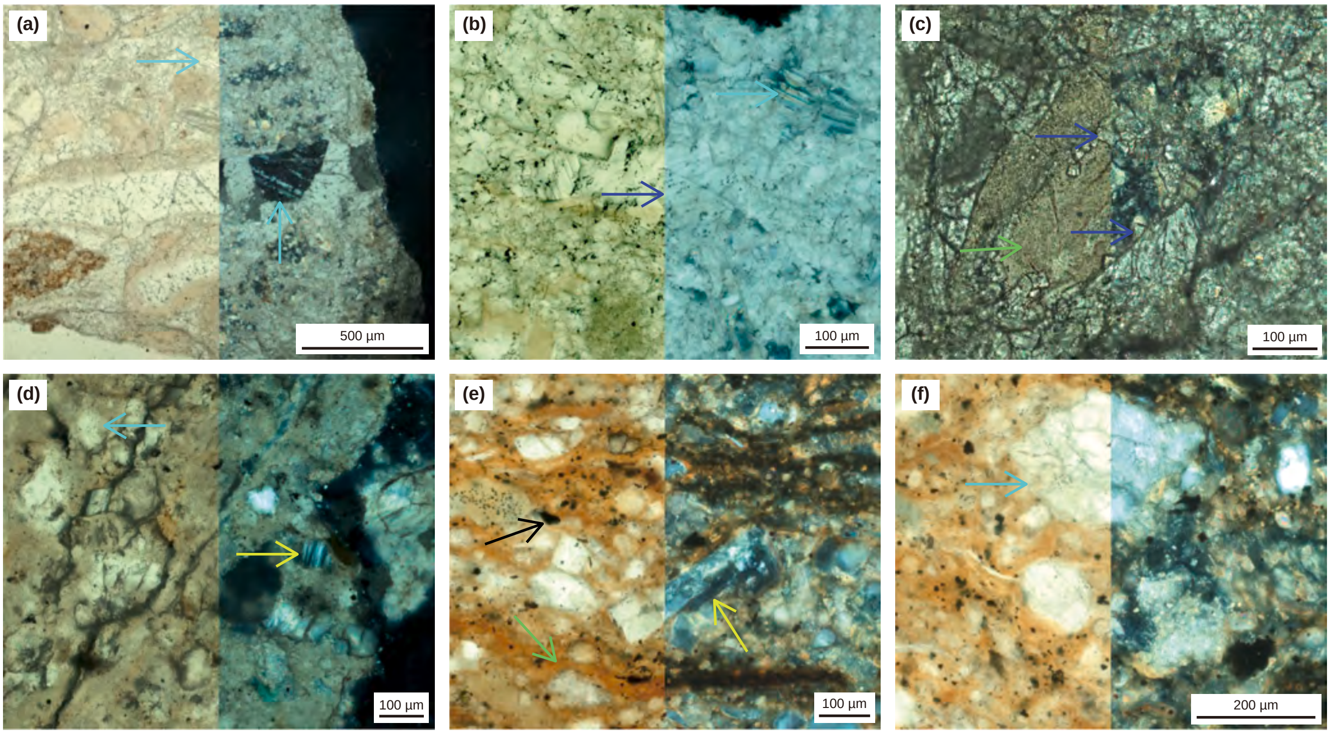


**Fig. 9.** Common diagenetic features observed under thin-section analysis. (**a**) Early diagenetic macrocrystalline calcite and blocky calcite (light blue arrow) cementing and replacing bioclastic fragments (probably bivalves); (**b**) dolomite cementing and replacing hybrid rock (blue arrow) and blocky calcite (light blue arrow); (**c**) subhedral to euhedral dolomite (blue arrow) over saponite peloids (green arrow); (**d**) microcrystalline calcite (light blue arrow) and labradorite grain (yellow arrow); (**e**) orthoclase partially dissolved (yellow arrow), saponite layers (green arrow), and opaque minerals (probably pyrite) mainly disposed over saponite (black arrow); (**f**) blocky calcite (light blue arrow).

networks (Fig. 8(e)); or subhedral to euhedral cubic crystals smaller than 200 μm (Fig. 8(f)).

Silica is typically observed as microcrystalline quartz, commonly associated with carbonate rocks where it infills intraparticle and moldic porosity, notably in fragmented bioclastic packstones (Fig. 8(h)). In certain intervals, pervasive silicification obliterates original rock fabrics (Fig. 8(g)).

Saponite (Fig. 8(i)) originates from the alteration of precursor minerals such as feldspar and mica and occurs as thin, crenulated, subparallel laminae or as small granular aggregates. Locally, saponite shows interstratification with illite (I/S), evidenced by its glycolated reflection at 8.2 Å (Fig. 4). Both saponite and saponite–illite interstratifications are exclusive to the Piçarras Formation.

## 5. Discussion

### 5.1. Geophysical well log interpretations

Geophysical well logs record continuous variations in physical parameters along boreholes and are fundamental tools in subsurface characterization (Rider, 2002; Ellis and Singer, 2007; Carrasquilla and Lima, 2020; Lai et al., 2023, 2024). When acquired during drilling, the technique is referred to as LWD, whereas measurements collected after the drill string has been pulled out are known as WL.

Among the multiple applications of well logs, their use for lithology and lithofacies prediction is particularly significant, as it enables extrapolating petrological information from the scale of cutting samples to the well scale (Nabawy and Géraud, 2016; He et al., 2019; Lai et al., 2024). Logs such as gamma ray, resistivity, sonic, density, neutron, photoelectric factor, and nuclear magnetic resonance are essential tools for these analyses (Lai et al., 2024; Keeton et al., 2015; Brekke et al., 2017).

Moreira et al. (2007) and Leite et al. (2020) observed a pronounced shift in density log values at the contact between the Piçarras and Itapema formations, attributing the lower densities in the Piçarras Formation to higher contents of Mg-rich clays. This study further investigates geophysical log signatures that reflect the lithogeochemical and mineralogical properties of the Piçarras Formation.

The GR log measures natural radioactivity, primarily reflecting the presence of isotopes such as $^{40}K$, $^{232}Th$, and $^{238}U$, and is widely used for lithological identification and clay content estimation (Nery, 2005; Ellis and Singer, 2007; Lai et al., 2024). Clay minerals and fine sediments tend to concentrate radioactive elements, and heavy metals can become preferentially associated with these fine particles (Bassiouni, 1994).

In the Piçarras Formation, elevated GR values correspond to higher siliciclastic input, particularly from K-feldspar and clay content (Fig. 2, Table 4). Conversely, carbonate-rich intervals exhibit lower GR readings. Strong positive correlations between GR and minerals such as plagioclase and pyrite (Supplementary S9) likely reflect indirect associations, as these minerals frequently co-occur with K-feldspar and clay content in the sediment matrix.

RES logs are influenced not only by the intrinsic electrical properties of rocks but also by porosity, fluid salinity, borehole conditions, and the presence of conductive minerals such as clays and sulfides (Rider, 2002; Ellis and Singer, 2007). LWD systems commonly employ electromagnetic wave resistivity (EWR) tools, which rely on wave propagation affected by formation conductivity, dielectric permittivity, and magnetic permeability, governed by Maxwell's equations (Olhoeft, 1981).

These physical principles imply that EWR measurements are sensitive not only to bulk rock properties but also to subtle effects caused by mineral composition, surface conduction, and bound water in clay minerals. Although mica behaves as an electrical insulator under ideal conditions, it can lower resistivity in natural settings due to its association with conductive ions, clays, pore fluids, and surface conduction phenomena (Winsauer and McCardell, 1953; Wyllie and Southwick, 1954; Vinegar and Waxman, 1984). In low-porosity environments, the influence of clays and surface conduction becomes particularly significant (Vinegar and Waxman, 1984; Garrouch and Sharma, 1994; Glover et al., 1994). The combined presence of mica and saponite accentuates this resistivity-lowering effect, as saponite's surfaces host mobile interlayer cations (Bockris et al., 2000; Qi and Wu, 2022). These ions contribute to interfacial polarization, delaying the electrical response during field changes and producing phase shifts in electromagnetic waves, ultimately reducing the apparent resistivity measured by the tool (Vinegar and Waxman, 1984; Gunderson et al., 2000; Boadu and Seabrook, 2006). This theoretical behavior is directly reflected in well 1-BRSA-1363-RJS, where resistivity values drop sharply to ~1.8 Ω·m in intervals rich in mica and saponite (yellow arrows, Fig. 2). These low-resistivity zones coincide precisely with lithofacies containing high concentrations of Mg-rich clays (Table 4, Supplementary S9), confirming that surface conduction and interlayer cations in these minerals significantly influence the electrical log responses in the Piçarras Formation.

DTCO and DTS record the travel time of compressional and shear waves, providing valuable information about porosity, lithology, fluid content, fracturing, and overpressure zones (Ellis and Singer, 2007; Liu, 2017; Bateman, 2020). Lower transit times indicate higher velocities, typically associated with more rigid and less porous rock matrices (Rider, 2002; Ellis and Singer, 2007). In the Piçarras Formation, sonic logs show increased slowness in zones with higher mica content (blue arrows, Fig. 2, Table 4), suggesting reduced acoustic velocity due to mica's platy structure and preferred orientation. Saponite exhibits a weaker correlation with slowness (Supplementary S9), indicating a more modest impact on acoustic properties.

RHOZ measures bulk density by detecting gamma rays scattered from interactions induced by a $^{137}$Cs source (Rider, 2002; Ellis and Singer, 2007). Due to its sensitivity to borehole irregularities, density measurements require corrections using caliper logs (Bond et al., 2010). Lower apparent porosity in dolomitic rocks is attributed to dolomite's higher grain density compared to calcite (KGS, 2017).

PEF log, acquired with the same tool as the density log, measures the absorption of low-energy gamma rays, providing values related to the atomic number of absorbing elements (Rider, 2002; Ellis and Singer, 2007). Elements such as Ba in barite (PEF = 267 b/electron) can strongly influence readings in enlarged borehole intervals (Rider, 2002; De Oliveira et al., 2024). In well 1-BRSA-1363-RJS, a moderate correlation between PEF and barite content (Supplementary S9) suggests that elevated PEF values may result from barite contamination but also from higher saponite concentrations due to its iron content.

Neutron logs (NPOR) determine porosity based on hydrogen content by recording gamma rays produced after neutron capture (Asquith and Krygowski, 2004; Nery, 2005; Ellis and Singer, 2007). In clean formations, neutron porosity reflects fluid-filled pore spaces; however, clays can elevate readings through their bound water and hydroxyl groups (Bhuyan and Passey, 1994).

Although the neutron log encompasses only the upper 30 m of the Piçarras Formation, it demonstrates the highest correlation among all geophysical logs analyzed (Supplementary S9). In zones where saponite is present, neutron porosity measurements exceed the actual formation porosity (Fig. 2). This discrepancy is attributed to the hydrogen contained within the clay structure and its associated bound water. The strong correlation observed between mica and the neutron log (Supplementary S9) may be explained by the presence of $K^+$ cations, which form stable interlayer bonds that retain hydroxyl groups within the octahedral layers of the mica structure. Given that saponite originates from the diagenetic alteration of detrital minerals, the observed correlations are consistent with the documented mineralogical evolution. Despite the use of a compensated neutron log in this study, which minimizes borehole effects through dual detectors (Asquith and Krygowski, 2004), the moderate correlation observed with barium (Spearman = 0.42; Supplementary S9) suggests that the hydrogen content of the drilling fluid may still exert some influence on the measurements.

NMR logging provides detailed insights into fluid distribution, total and bound fluid volumes, hydrocarbon identification, intrinsic permeability, and pore size distributions (Luthi, 2001; Tan et al., 2014; Liu, 2017; Olatinsu et al., 2017; Wang et al., 2020). A key advantage of NMR is its ability to distinguish clay-bound and capillary-bound fluids from movable fluids (Asquith and Krygowski, 2004). In the Piçarras Formation, high $NMR_{CBW}$ volumes correlate with abundant clay minerals (Fig. 2), as similarly observed in other basins and formations (Clavier et al., 1984; Alansari et al., 2019; Abid et al., 2025). Although direct correlations between $NMR_{CBW}$ and individual minerals such as saponite, mica, and plagioclase are weak, NMR logs show a clear increase in clay-bound water volumes below 6000 m, coinciding with saponite-rich intervals and its microporous structure (Fig. 2, Asquith and Krygowski, 2004).

### *5.2. Understanding the nature of the contact between Piçarras and Itapema formations*

Previous studies have demonstrated that the Piçarras and Itapema formations were deposited under distinct climatic and hydrochemical conditions (Moreira et al., 2007; Leite et al., 2020). The Piçarras Formation developed under highly alkaline conditions, transitioning to less alkaline environments in the Itapema Formation, likely driven by a more humid climate and tectonic deepening of the lacustrine system, which favored bivalve proliferation (Leite et al., 2020).

The upper boundary of the Piçarras Formation is regionally defined by the Pré-Jiquiá (Intrabarremian) Unconformity at approximately 126.4 Ma (Moreira et al., 2007). In well 1-BRSA-1363-RJS, this boundary is identified at a depth of 6000 m, corresponding to the first interval where saponite is entirely absent from cutting samples (Fig. 3). Below this depth, saponite is abundant and closely associated with laminated siliciclastic and carbonate mudstones, reflecting alkaline, low-energy lacustrine conditions. Above this boundary, within the Itapema Formation, saponite is absent, indicating a pronounced change in paleoenvironmental conditions, lithofacies composition, and mineral assemblages.

Three key features characterize this contact (Fig. 3). Mineralogically, saponite ($d_{001}$ reflection near 15 Å) is absent in the Itapema Formation, attributed to shifts in climate as well as decreased salinity and alkalinity (Leite et al., 2020; Amorim et al., 2024). Divergence between quartz and silicon geochemical curves indicates increased siliciclastic input during Piçarras deposition, corroborated by orthoclase, quartz, mica, and plagioclase identified in XRD analyses (Table 4). Additionally, variations in dolomite and magnesium contents suggest an additional Mg source linked to saponite.

Geophysical logs further support this interpretation: in the Piçarras Formation, lower resistivity and density coincide with higher sonic slowness, neutron porosity, and $NMR_{CBW}$ volumes (Fig. 2). These signatures align with elevated Mg-rich clay concentrations in Piçarras siliciclastic intervals.

Overall, the contrasting geophysical, mineralogical, and geochemical data strongly indicate that the Piçarras and Itapema formations were deposited under markedly different paleoenvironmental conditions. The disappearance of saponite, shifts in trace element affinities, and increased microporosity reflected in clay-bound water volumes all support the interpretation of an abrupt contact. Regionally, the Pré-Jiquiá (Intrabarremian) Unconformity (Moreira et al., 2007) likely contributed to truncating the sedimentary record, juxtaposing deposits indicative of significantly different depositional settings.

### *5.3. A paleoenvironmental and paleoclimate model for the Piçarras Formation*

In continental basins, absolute accommodation is primarily governed by basin topography and sediment accumulation rates (Carroll and Bohacs, 1999; Lin et al., 2001). Changes in basin morphology and the distribution of sediment sources and depocenters are largely dictated by tectonic processes (Hou et al., 2020). Once a topographic depression is established through tectonic activity, lake development and evolution become strongly influenced by climatic conditions, which are critical in determining the depositional style of lacustrine systems (Olsen, 1990; Kreuser, 1995). Lacustrine environments are highly sensitive to variations in hydrological balance, with lake levels and volumes responding closely to regional climate oscillations (Hou et al., 2020; Xu et al., 2019; Qin et al., 2021).

Carbonates are common in lacustrine rift-fill successions (Ashley and Renault, 2002), and their deposition reflects hydrological conditions, groundwater geochemistry, sedimentation rates, and atmospheric composition, making them sensitive indicators of climatic, tectonic, and base-level changes (Platt and Wright, 1991; Alonso-Zarza and Wright, 2010a, 2010b; Gomes et al., 2020; Jewuła et al., 2023). Seasonal variations in organic productivity, precipitation, mineral redissolution, and detrital influx can produce finely laminated carbonate beds, preserved under anoxic conditions due to the absence of bioturbation (Verrecchia, 2008). The most productive continental carbonate systems typically develop under semi-arid conditions, where limited rainfall reduces siliciclastic influx while maintaining sufficient water for dolostone or limestone formation (de Wet et al., 2015; Hou et al., 2020). In contrast, humid conditions increase water and sediment supply, while deeper lakes promote stratification and organic matter preservation (Bates, 1953; Lerman, 1978; Mulder and Alexander, 2001; Hou et al., 2020). Clastic input in rift environments and lacustrine systems often reflects the relief generated by thermal uplift and block faulting, which enhances erosion and sediment transport (Tucker and Jones, 2023).

Föllmi (2012) describes the interval from the late Barremian to early Aptian as a period of significant climatic and environmental transitions, marked by episodes such as the Taxy and Selli events. The Taxy and Selli events are dated approximately between 126 and 123 Ma, spanning the latest Barremian to the earliest Aptian interval (Föllmi, 2012). During shifts from arid to more humid conditions, basins that had previously experienced desiccation due to high rates of evapotranspiration could become recharged with water, leading to extensive lacustrine development (Föllmi, 2012). Similar climatic influences have been documented in rift basins worldwide, including East Asia, Central Africa, South America, and southern Europe (Ito et al., 2006; Harris et al., 2004; Heimhofer et al., 2010).

These documented global climate perturbations provide an essential framework for evaluating the depositional history of the Piçarras Formation. Although precise chronological constraints are lacking, several features observed in well 1-BRSA-1363-RJS, including episodic siliciclastic influxes, shifts in Mg-clay deposition, and changes in chemofacies, could reflect responses to such climatic perturbations. Establishing definitive correlations, however, remains challenging and requires further integration of high-resolution geochronological and chemostratigraphic data.

In the context of well 1-BRSA-1363-RJS, the facies evolution of the Piçarras Formation was strongly influenced by climate fluctuations (Fig. 10), shaping sediment dispersal patterns. The succession is dominated by interbedded very fine-grained siliciclastic mudstones, lime mudstones, and laminites (Fig. 11). Notably, at a depth of 6,012 m, a coarse-grained hybrid rock was observed (Fig. 6(k) and (l)), likely reflecting the combined effects of tectonic and climatic influences (Hou et al., 2020). Within a regionally arid climate (Chumakov et al., 1995; Dias, 2005; Moreira et al., 2007; Boucot et al., 2013; Hay and Floegel, 2013), carbonate sedimentation in Lake Piçarras is interpreted as characteristic of the driest periods, when minimal allogenic sediment was supplied. This carbonate deposition was interrupted four times by significant siliciclastic influxes, probably induced by climatic shifts toward wetter conditions (Potter et al., 2005; Tucker and Jones, 2023), which increased precipitation and sediment delivery to the lake (Bates, 1953; Lerman, 1978; Mulder and Alexander, 2001) (Fig. 12(b)).

The fine-grained, laminated nature of these deposits suggests sedimentation in relatively deep-water environments (Fig. 12(a)), below the influence of wave and current action (Thomas et al., 1972, 1973; Lerman, 1978; Cohen, 2003; Tucker and Jones, 2023; Flügel, 2004; Muniz, 2014). During drier intervals (Fig. 12(c)), carbonate deposition was dominant and coincided with lake regressions (Brunskill, 1969; Thomas et al., 1972; Lerman, 1978; Potter et al., 2005; Tucker and Jones, 2023). Less arid phases (Fig. 12(b)) instead promoted lake transgressions and increased sediment influx via hypopycnal flows (Bates, 1953; Mulder and Alexander, 2001; Potter et al., 2005; Tucker and Jones, 2023), followed by settling from suspension.

Although no formal geochemical proxies were applied in this study to quantify arid versus humid paleoclimatic conditions, the integration of mineralogical and geochemical data revealed that intervals interpreted as more humid coincide with increased concentrations of detrital indicators such as Zr, $TiO_2$, and $Al_2O_3$ (chemofacies Q1 in Fig. 10). These elements reflect enhanced siliciclastic input, likely associated with intensified fluvial runoff during wetter periods (Lauterbach et al., 2011; Marshall et al., 2011; Kämpf et al., 2012; Corella et al., 2012; Davies et al., 2015).

While the Piçarras Formation records significant paleoenvironmental variability, it remains uncertain whether the observed sedimentary and mineralogical transitions can be precisely correlated with global events such as the Taxy and Selli. Nevertheless, the timing and nature of increased siliciclastic input and shifts in Mg-clay deposition suggest a potential link to these climatic episodes, warranting further investigation. If confirmed through high-resolution dating and chemostratigraphy, these mineralogical and geochemical signals could serve as valuable regional markers for correlating the Piçarras Formation with broader Barremian–Aptian climatic perturbations.

A reliable indicator of alkaline lacustrine conditions is the occurrence of Mg-rich clay minerals (Darragi and Tardy, 1987; Pozo and Galán, 2015; Calvo and Pozo, 2015; Salgado-Campos et al., 2022). The abundant saponite observed in the Piçarras Formation (Table 4, Fig. 3) suggests deposition under highly alkaline and brackish conditions (Pozo and Casas, 1999; Tosca, 2015; Leite et al., 2020; Salgado-Campos et al., 2022). The incorporation of $Al^{3+}$ into the saponite structure likely originates from the alteration of Al-bearing minerals such as feldspar and mica (Pozo and

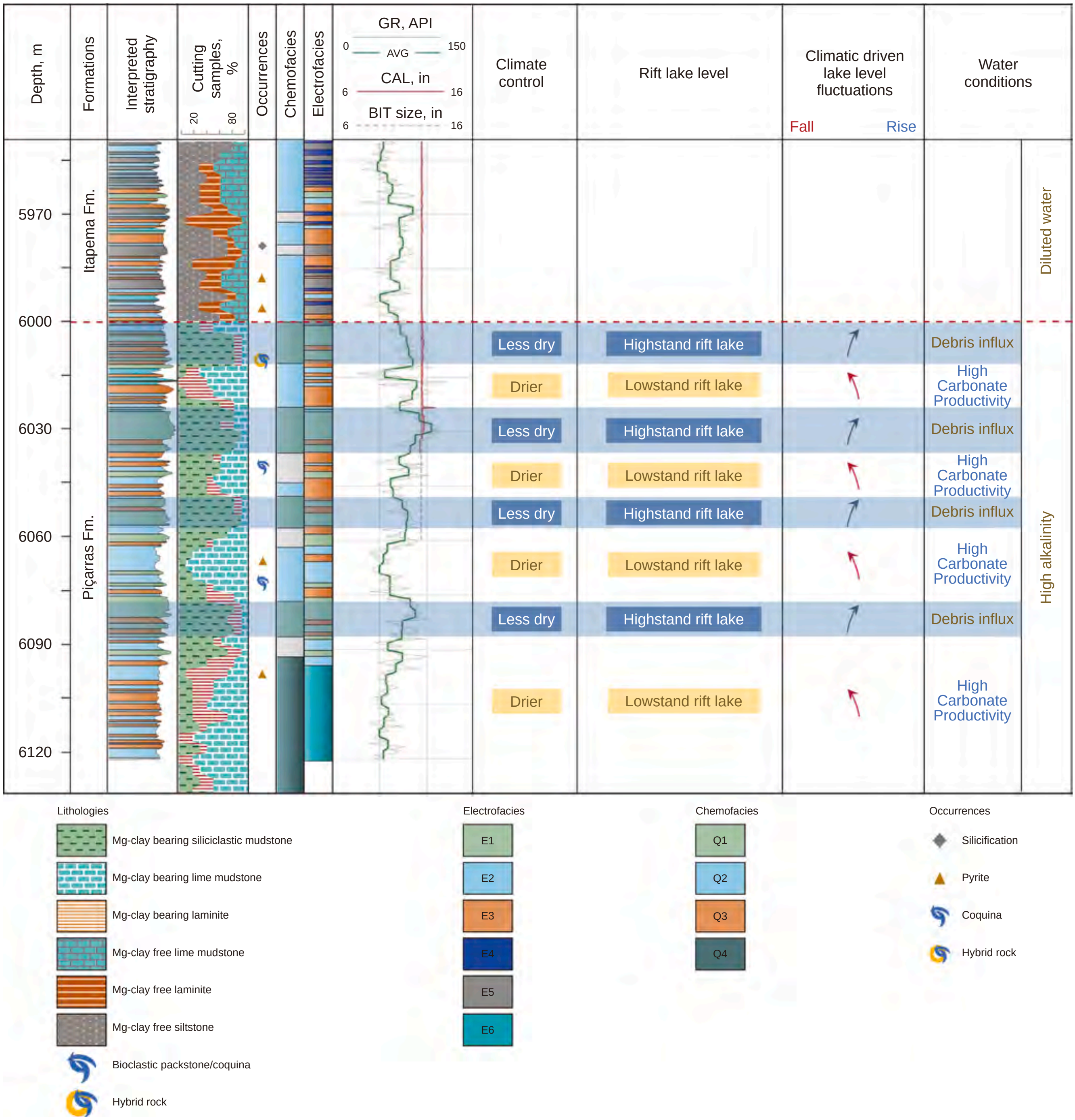


**Fig. 10.** Climatically driven lake-level fluctuations during the Barremian caused debris influx into the Piçarras Formation. In the climatic driven lake level fluctuations track, blue arrows indicate transgressions, and red arrows indicate regressions. Less arid periods correspond to chemofacies Q1, characterized by increased concentrations of $TiO_2$ and $Al_2O_3$. These elements are indicative of higher detrital input, commonly associated with enhanced fluvial runoff during wetter climatic phases.

Calvo, 2018), both abundant in the analyzed samples (Table 4, Figs. 3 and 9).

Two principal hypotheses address the source of magnesium in the Piçarras Formation: (1) weathering of mafic to ultramafic rocks in the source area; or (2) syngenetic hydrothermal processes. Hydrothermal activity can enrich sediments in elements such as Cu, Zn, and Pb, sometimes up to 40 times higher than Post-Archean Australian Shale (PAAS) values, and elevate REE contents (Salgado-Campos et al., 2022). In the Piçarras Formation, Cu enrichment is noted but limited to a factor of two compared to PAAS (Table 5), suggesting a sedimentary rather than hydrothermal origin. Zn and Pb levels cannot be conclusively assessed due to their association with barium and barite (Supplementary S9) and potential contamination from drilling fluids. Given that the Piçarras Formation lies directly above the basaltic Camboriu Formation, a source-area origin for Mg appears more plausible, although a hydrothermal contribution cannot be entirely excluded.

The sample from 6012 m exhibits a distinct sedimentological signature, consisting of a massive hybrid texture with rounded, medium-grained saponite peloids interspersed with fragmented

| | Facies | Code | Name | Description | Interpretation |
|---|---|---|---|---|---|
| Mg-clay bearing facies | 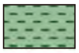 | Mg-$S_M$ | Mg-clay bearing laminated siliciclastic mudstone | Dark olive green slightly carbonatic very-thin plane-parallel laminated siliciclastic mudstone. Observed discontinuous 10 to 20 μm thin laminations, alternating dark olive green and light gray colors. Occur silty size (10 μm) heavy minerals dots and disseminated or solely pyrite. Mineralogy composed of K-feldspar (mainly orthoclase), mica (biotite and muscovite), quartz, plagioclase (mainly labradorite), pyrite and saponite. | Fine allochthonous siliciclastic grains enter the lake in hypopycnal plumes, associated with high lake levels (Bates, 1953; Mulder and Alexander, 2001), and are deposited by settling at the lake bottom (Carvalho et al., 2000; Oliveira et al., 2019). This process occurs under conditions of high alkalinity in a lacustrine environment (Pozo and Casas, 1999; Herlinger et al., 2017). |
| Mg-clay bearing facies |  | Mg-$L_M$ | Mg-clay bearing laminated to massive lime mudstone | White smoke to light gray, massive to slightly laminated lime mudstone. Anhedral to subhedral dolomite, kerogen and disseminated pyrite. Saponite in laminations under submilimetric scale. Mineralogy composed of calcite, dolomite, quartz, pyrite, saponite and less amount of K-feldspar (mainly orthoclase). | Facies formed in low-energy lakes with calcium available in solution. These facies may be associated with relatively deeper or more protected areas, below the storm wave base (Flügel, 2004; Muniz, 2013), under conditions of high alkalinity in a lacustrine environment (Pozo and Casas, 1999; Herlinger et al., 2017). |
| Mg-clay bearing facies |  | Mg-$L_{AM}$ | Mg-clay bearing laminite | Bronze brown laminite, showing a 50 micrometers thick discontinuous smooth wavy lamination. The light brown Mg-clay levels may show a degree of replacement by dolomite. Mineralogy composed of calcite, dolomite, quartz, saponite, K-feldspar (mainly orthoclase) and plagioclase (mainly labradorite). | High-frequency rhythmic lamination facies associated with solar cycles (Andrews et al., 2010; Andrews and Hartley, 2015; in Tucker & Jones, 2023), characteristic of deep-water lacustrine deposits (Tucker & Jones, 2023). This process occurs under conditions of high alkalinity in a lacustrine environment (Pozo and Casas, 1999; Herlinger et al., 2017). |
| Mg-clay free facies |  | $L_M$ | Mg-clay free laminated to massive lime mudstone | White smoke to light gray, massive to slightly laminated lime mudstone. Anhedral to subhedral dolomite, kerogen and disseminated pyrite. Mineralogy composed of calcite, dolomite, quartz, pyrite and less amount of K-feldspar (mainly orthoclase). | Facies formed in low-energy lakes with calcium available in solution. These facies may be associated with relatively deeper or more protected areas, below the storm wave base (Flügel, 2004; Muniz, 2013). |
| Mg-clay free facies | 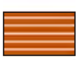 | $L_{AM}$ | Mg-clay free laminite | Bronze brown laminite, showing a 50 micrometers thick discontinuous smooth wavy lamination. Mineralogy composed of calcite, dolomite, quartz, K-feldspar (mainly orthoclase), mica (biotite and muscovite), and plagioclase (mainly labradorite). | High-frequency rhythmic lamination facies associated with solar cycles (Andrews et al., 2010; Andrews and Hartley, 2015; in Tucker & Jones, 2023), characteristic of deep-water lacustrine deposits (Tucker & Jones, 2023). |
| Mg-clay free facies |  | S | Mg-clay free siltstone | Weak-laminated siltstone characterized by its light to orangish grey color. Mineralogy composed of calcite, dolomite, quartz, K-feldspar (mainly orthoclase), plagioclase (mainly labradorite) and mica (biotite and muscovite). | Fine allochthonous siliciclastic grains enter the lake in hypopycnal plumes related to high lake levels (Bates, 195; Mulder and Alexander, 2001), and are deposited by settling at the lake bottom (Carvalho et al., 2000; Oliveira et al., 2019). |
| Rare lithologies occurring under 1% as isolated cutting sample fragments |  | C | Packstone bioclastic (coquina) | Locally, cutting samples show rare (less than 1%) dispersed fragments of grainstone/coquina with broken and disarticulated bioclasts. These rare coquina fragments are white smoke to light gray with low porosity and silicified matrix. | Facies deposited during low lake level periods, where the carbonate mud was partially remobilized by weak currents or wind-generated waves (Bertani & Carozzi, 1985). |
| Rare lithologies occurring under 1% as isolated cutting sample fragments |  | $H_R$ | Hybrid rock | Locally, at the depth 6012 m, were observed rare (less than 1%) fragments of hybrid rock formed by a mixture of broken/disarticulated bioclasts and fine sand sized Mg-clay (saponite) peloids. | Sediments from the shallower regions of the lake were mixed by gravity redeposition or storm-induced currents (Leite et al., 2020). |

**Fig. 11.** Lithologies characterized in cutting samples from both the Itapema and Piçarras formations and their environmental interpretations.

and disarticulated bivalve shells (Fig. 9(a)–(c)). This facies suggests redeposition by gravity flows (Goldberg et al., 2017; Leite et al., 2020), followed by hydraulic reworking through traction currents (Kidwell and Bosence, 1991). Such gravity-driven processes were probably triggered by storm events or tectonic disturbances that mobilized shallower deposits and transported them into deeper lacustrine settings (Leite et al., 2020).

### *5.4. Diagenetic patterns based on macroscopic and microscopic petrography*

Diagenesis encompasses the physical and chemical processes that affect sedimentary materials after deposition but before weathering or metamorphism (Milliken, 2003). Several authors have emphasized the close relationship between syngenetic and eodiagenetic processes (Herlinger et al., 2017; Lima and De Ros, 2019; Sartorato et al., 2020; Wright and Barnett, 2020; Carvalho et al., 2022). Early diagenesis involves chemical reactions occurring under temperatures below 70 °C, at shallow burial depths and near the sediment-water interface (Curtis, 1995; Taylor, 1998; Zhu et al., 2020; Wang et al., 2024), whereas mesodiagenesis takes place at temperatures above 70 °C (Burley, 1993; Wang et al., 2024).

Compaction is widely recognized as the principal diagenetic mechanism in shale formations dominated by extrabasinal particles (Milliken et al., 2019). Sodium-rich K-feldspar and calcium-

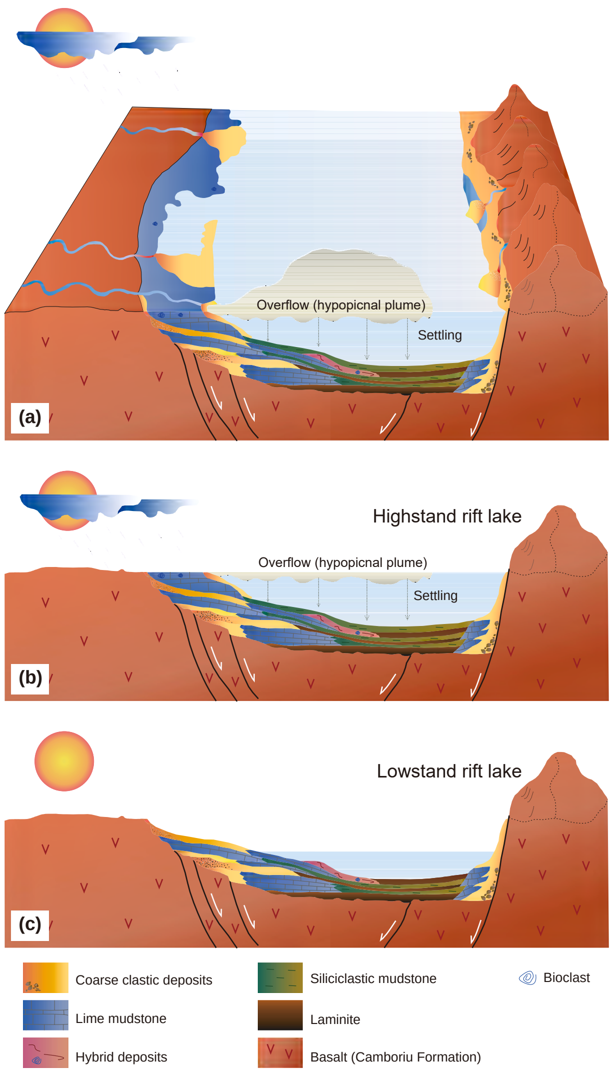


**Fig. 12.** Depositional model for the Piçarras Formation illustrating sediment accumulation and depositional facies in a climate-controlled highstand and lowstand rift lake. (**a**) Simplified conceptual model illustrating the lake where Piçarras Formation rocks were deposited, representing the rift phase environment; (**b**) idealized highstand rift lake, where hypopycnal plumes reach the lake during less arid periods, transporting sediments into deeper lake areas where they settle from suspension; (**c**) idealized lowstand rift lake during more arid periods, where carbonate rocks predominate.

rich detrital plagioclase grains are more susceptible to dissolution and replacement than K-rich K-feldspar or sodium-rich plagioclase (Maynard, 1984; Milliken, 1988; Milliken, 1992; Milliken, 1989).

In the Piçarras Formation, diagenetic processes include calcite cementation, pyritization, dolomitization, silicification, transformation of precursor Al-bearing minerals into saponite, and illitization of saponite forming interstratified illite-smectite (Fig. 8).

The Piçarras Formation developed atop the basaltic Camboriu Formation. Lakes formed on volcanic terrains commonly host calcite and trioctahedral smectites (Cerling, 1994; Leite et al., 2020), a process facilitated by hydrothermal fluids and/or basalt weathering, which supply $Na^+$, $Ca^{2+}$, $HCO_3^-$, Si, and Mg to lake waters (McKinley et al., 1999). Abundant early diagenetic precipitation of macrocrystalline, blocky calcite (Fig. 9(f)), acting both as cement and replacive mineral for bioclastic fragments (Fig. 9(a)), is associated with elevated calcium concentrations in lake and interstitial waters resulting from carbonate alteration and dissolution. The coarse crystal size of early calcite cement is likely related to the brackish nature of both lake water and pore fluids (Leite et al., 2020).

Disseminated microcrystalline pyrite likely formed under anoxic conditions through bacterial sulfate reduction (Berner, 1984; Westrich and Berner, 1984; Holmer and Storkholm, 2001; Leite et al., 2020; Wang et al., 2024), increasing fluid alkalinity and facilitating dolomitization beneath the sulfate reduction zone (Morad, 1998; Curtis, 1980). Macrocrystalline euhedral pyrite (Fig. 8(f)) in the Piçarras Formation is associated with thermal sulfate reduction during mesodiagenesis (Raiswell, 1982; Berner, 1984; Worden et al., 2003; Leite et al., 2020). High concentrations of opaque minerals, including pyrite, occur alongside saponite layers (Fig. 9(e)), as saponite can supply Fe for pyrite formation. Pyrite's association with clay- and silt-rich mudstones is linked to slow-to-moderate sedimentation rates, Fe-rich pore waters, and high organic matter content during early diagenesis (Taylor and Macquaker, 2018).

Dolomite is a well-documented diagenetic mineral in pre-salt sequences (Herlinger et al., 2017). Dolomitization involves the replacement of limestone via dissolution-precipitation processes facilitated by Mg-rich fluids (Zhang et al., 2022). Two dolomitization patterns are identified: (1) pervasive replacement (Fig. 8(b) and (c)) and (2) pore-filling dolomite (Fig. 8(a)), both favored by alkaline lake waters and early diagenetic conditions. According to Herlinger et al. (2017), pervasive replacement is often linked to silicification and fracturing, suggesting possible hydrothermal fluid circulation. Macrocrystalline dolomite replacing grains and interparticle cements may also result from thermal decarboxylation during mesodiagenesis (Surdam and Crossey, 1985; Morad, 1998; Leite et al., 2020). Additionally, Glenn and Kelts (1991) proposed that diagenetic processes can impart laminations or rhythmic textures to lake deposits, with early dolomite forming close to the sediment-water interface.

Silica diagenesis can involve transformations among various solid silica phases in siliceous sediments during shallow to intermediate burial, or the silicification of non-siliceous rocks, which may range from localized to pervasive (Hesse, 1989). Potential silica sources for quartz cementation include silica released during smectite-to-illite conversion (Peltonen et al., 2009; Day-Stirrat et al., 2010; Thyberg et al., 2010), dissolution of siliceous skeletal debris (Schieber et al., 2000; Milliken et al., 2016; Taylor and Macquaker, 2018), feldspar alteration, pressure dissolution of detrital quartz, and volcanic ash (Williams et al., 1985). Two geochemical pathways appear relevant for the diagenetic silica observed in the analyzed samples. The pervasive silicification by cryptocrystalline silica (Fig. 8(g)) likely represents silica-replaced carbonates (Hesse, 1989). In this process, silica is dissolved from detrital silicates (mainly quartz and feldspar) by alkaline lake waters (pH 9.5–10.2) and subsequently precipitates as pH decreases during evaporation and increased hypersalinity (Hesse, 1989). Silica filling interparticle and intraparticle pores in bioclastic packstones (Fig. 8(h)) is attributed to hydrothermal fluids (Leite et al., 2020), as documented in the rift sequences of the Campos Basin (Goldberg et al., 2017; Herlinger et al., 2017).

In the Piçarras Formation, intermediate diagenesis is characterized by clay mineral transformations. A gradual conversion of smectite into interstratified smectite-illite (I/S) occurs at temperatures between 60 and 140 °C (Freed and Peacor, 1989; Wang et al., 2024). As this process requires Al and K (Worden and Morad, 1999), and given the relative immobility of Al (McKinley et al., 1999), dissolution and albitization of K-feldspar (Fig. 9(e)) are considered the main sources of potassium, with the released silica precipitating locally within mudstones (Towe, 1962; Awwiller, 1993; Abercrombie et al., 1994; Peltonen et al., 2009; Thyberg et al., 2010; Wang et al., 2024).

*5.5. Applications for the oil and gas industry*

Operational insights gained from mineralogical, lithogeochemical, petrographic, and geophysical analyses are as crucial as scientific interpretations, as they inform decision-making and help optimize well operations. Challenges frequently arise during drilling due to the chemical and structural characteristics of the rocks being penetrated (Vidal et al., 2022; Gonzaga et al., 2024). Interactions between drilling fluids and the drilled rocks are common and involve both physical and chemical processes (Stuckman et al., 2019). Mechanical alterations caused by stresses from the drill bit and drill string components (Peretomode et al., 2022), as well as stability problems resulting from rock strength limitations (Araujo et al., 2020), or mineral hydration and swelling upon exposure to water-based drilling fluids (Anderson et al., 2010), are significant operational concerns. Accurately identifying lithologies or formation boundaries is essential for decisions regarding drilling interruptions for phase changes, well abandonment, or adjustments in drilling parameters to enhance penetration rates (Gonzaga et al., 2024; Leon et al., 2024).

Differentiating the Piçarras and Itapema formations has long posed operational challenges. Macroscopic petrographic analysis of cuttings is complicated by the small size of fragments produced by the drill bit. Identifying bioclasts, even when fragmented or disarticulated, remains difficult during cuttings analysis, despite their potential as stratigraphic markers. However, lithogeochemical, mineralogical, and geophysical analyses have revealed diagnostic signatures (Fig. 3) useful for distinguishing these formations, reflecting their distinct paleoenvironmental conditions.

In the 1-BRSA-1363-RJS well, the exclusive occurrence of saponite in the Piçarras Formation (Table 4, Fig. 3) provides a reliable criterion for identifying this unit. Other minerals detected by X-ray diffraction do not offer comparable diagnostic utility. Saponite increases clay-bound water in the nuclear magnetic resonance log through water adsorption (Fig. 3). Additionally, the presence of mica contributes to reductions in sonic velocities, reflected as increased DTCO and DTS slowness. Resistivity readings are also reduced due to the high cation exchange capacity of smectite and mixed-layer illite-smectite clays (Gunderson et al., 2000), while neutron log readings rise, not as a true increase in porosity but as a manifestation of the shale effect (Fig. 2) (Asquith and Krygowski, 2004).

The significant swelling behavior of clay minerals, particularly those in the smectite group like saponite, has been extensively documented (Chaaya et al., 2023). Such swelling presents operational risks when drilling with water-based fluids, potentially leading to stuck pipe or wellbore collapse (Anderson et al., 2010). Thus, predicting and identifying intervals containing smectite-type clays is critical for successful well completion. Moreover, divergences between MgO and dolomite trends, as well as between $SiO_2$ and quartz (Fig. 3), can assist in identifying the top of the Piçarras Formation during drilling operations.

## 6. Conclusions

- The integration of sedimentological, mineralogical, petrographic, geochemical, and geophysical well log data provided a comprehensive, high-resolution characterization of the Piçarras Formation in the 1-BRSA-1363-RJS well. This directly addressed the study's objective of distinguishing lithofacies assemblages and understanding their paleoenvironmental and diagenetic controls. The multidisciplinary approach enabled the identification of key lithologies, including laminated siliciclastic and carbonate mudstones, fragmented bioclastic packstones (coquinas), and hybrid resedimented rocks bearing Mg-clay minerals, and clarified their spatial distribution and geochemical signatures critical for reservoir prediction and stratigraphic correlation.
- Saponite was the only Mg-clay identified, occurring exclusively in the Piçarras Formation. It formed through syngenetic transformation of detrital precursors under alkaline, low-energy conditions and is closely associated with siliciclastic-dominated lithologies. Its complete absence in the overlying Itapema Formation reflects markedly different paleoenvironmental conditions.
- The fine-grained, laminated nature of the deposits supports deposition in a relatively deep lacustrine environment, below the influence of wave reworking. Climatic fluctuations led to alternating periods of lake-level expansion and contraction, promoting episodes of carbonate precipitation during drier intervals and enhanced siliciclastic input during less arid periods.
- The sedimentological and geochemical signals identified in the Piçarras Formation suggest potential links to global Barremian–Aptian climatic events, such as the Taxy and Selli episodes. Further integration of isotopic and chronostratigraphic data could strengthen these correlations and enhance understanding of regional responses to global climate shifts.
- Saponite occurrence is linked to elevated MgO concentrations and trace elements such as Cu, Co, and Ni, particularly in siliciclastic-rich intervals. This reinforces its interpretation as an authigenic product rather than a result of drilling contamination, as evidenced by its lack of geochemical association with barite and barium.
- Petrographic analyses revealed saponite as occurring in peloids, laminated aggregates, and granular forms, commonly altered to dolomite. Other diagenetic features observed include interstratification with illite, pervasive dolomitization, macrocrystalline and blocky calcite, pyrite, and quartz, indicating early to intermediate diagenetic stages under shallow burial conditions ($<140$ °C).
- The presence of saponite exerts a significant influence on geophysical log responses, manifesting as increased $NMR_{CBW}$ values, reduced resistivity, and variations in neutron and sonic measurements. When integrated with geophysical log data calibrated to cutting sample resolution, these effects directly contributed to achieving the study's objective of enhancing stratigraphic control. This integrated approach ultimately supports more precise formation identification and informed decision-making in Pre-Salt drilling operations, where operational performance and safety critically depend on accurate subsurface characterization.

## CRediT authorship contribution statement

**Jean Carlos Amorim:** Writing – original draft, Visualization, Validation, Resources, Methodology, Investigation, Formal analysis, Conceptualization. **Filipe Vidal:** Writing – review & editing, Visualization, Validation, Supervision, Methodology, Investigation, Conceptualization. **Reiner Neumann:** Writing – review & editing, Resources, Funding acquisition. **Carla Semiramis Silveira:** Writing – review & editing, Resources, Funding acquisition. **Cleverson Guizan Silva:** Writing – review & editing, Resources, Funding acquisition. **Fernando Freire:** Writing – review & editing, Visualization, Validation, Supervision, Resources, Project administration, Methodology, Investigation, Funding acquisition, Conceptualization. **Victor Salgado-Campos:** Writing – review & editing, Visualization, Validation, Supervision, Resources, Project administration, Methodology, Investigation, Funding acquisition, Conceptualization.

## Declaration of competing interest

The authors declares no conflicts of interest.

## Acknowledgments

The authors thank Petrobras for financing the R&D projects "*Projeto de estudo e análises em amostras de calha do Pré-sal e Margem Equatorial com ênfase em Operações Geológicas de Poços*" [project numbers: 2024/00103-9; 2024/00106-8], the Brazilian National Agency of Petroleum, Natural Gas and Biofuels (ANP) for providing the data used in this research, and BP Brasil for donating drilling cuttings from the 1-BRSA-1363-RJS well. Financial support from the Carlos Chagas Filho Foundation for Research Support of the State of Rio de Janeiro (FAPERJ) [grant numbers: E-26/210.354/2024] and the Brazilian National Council for Scientific and Technological Development (CNPq) [process #308035/2022-4] is also gratefully acknowledged. This work is part of the PhD research conducted by Jean Amorim within the Graduate Program in Ocean and Earth Dynamics (PPG-DOT) at Fluminense Federal University (UFF).

## Appendix A. Supplementary data

Supplementary data to this article can be found online at https://doi.org/10.1016/j.petsci.2025.12.022.

## References

Abercrombie, H.J., Hutcheon, I.E., Bloch, J.D., De Caritat, P., 1994. Silica activity and the smectite–illite reaction. Geology 22, 539–542. https://doi.org/10.1130/0091-7613(1994)022<0539:SAATSI>2.3.CO;2.

Abid, M., Ba, J., Markus, U.I., Tariq, Z., Ali, S.H., 2025. Modified approach to estimate effective porosity using density and neutron logging data in conventional and unconventional reservoirs. J. Appl. Geophys. 233. https://doi.org/10.1016/j.jappgeo.2024.105571.

Alansari, A., Salim, A.M.A., Janjuhah, H.T., Rahman, A.H.B.A., Fello, N.M., 2019. Quantification of clay mineral microporosity and its application to water saturation and effective porosity estimation: A case study from Upper Ordovician Sandstone reservoir, Libya. J. Nat. Gas Geosci. 4 (3), 139–150. https://doi.org/10.1016/j.jnggs.2019.04.005.

Alonso-Zarza, A.M., Wright, V.P., 2010a. Chapter 2, palustrine carbonates. In: Alonso-Zarza, A.M., Tanner, L.H. (Eds.), Carbonates in Continental Settings: Facies, Environments, and Processes. Elsevier, Amsterdam, pp. 103–132. https://doi.org/10.1016/S0070-4571(09)06102-0.

Alonso-Zarza, A.M., Wright, V.P., 2010b. Chapter 5, calcretes. In: Alonso-Zarza, A.M., Tanner, L.H. (Eds.), Carbonates in Continental Settings: Facies, Environments, and Processes. Elsevier, Amsterdam, pp. 225–267. https://doi.org/10.1016/S0070-4571(09)06105-6.

Amorim, J.C., Vidal, F.C., Freire, F., Campos, R.F., Borges, K.I.M., Salgado-Campos, V., 2024. Mineralogia, Quimiofacies e Eletrofacies da Formação Piçarras a partir das análises em amostras de calha e perfis do poço 1-BRSA-1363-RJS, Bacia de Santos. 51° Congresso Brasileiro de Geologia. https://doi.org/10.13140/RG.2.2.31688.12809.

Anderson, R.L., Ratcliffe, I., Greenwell, H.C., Williams, P.A., Cliffe, S., Coveney, P.V., 2010. Clay swelling–a challenge in the oilfield. Earth Sci. Rev. 98 (3–4), 201–216. https://doi.org/10.1016/j.earscirev.2009.11.003.

Andric, N., Sant, K., Matenco, L., Mandic, O., Tomljenovic, B., Pavelic, D., Hrvatovic, H., Demir, V., Ooms, J., 2017. The link between tectonics and sedimentation in asymmetric extensional basins: inferences from the study of the Sarajevo-Zenica Basin. Mar. Petrol. Geol. 83, 305–332. https://doi.org/10.1016/j.marpetgeo.2017.02.024.

Araujo, R.M.S., Fontoura, S.A.B., Marchesi, V.R., Domingues, D.L.P., Gonçalves, C., 2020. Metodologia para a Estimativa de Resistência de Rochas Carbonáticas Análogas ao Pré-sal Brasileiro. XX Congresso Brasileiro de Mecânica dos Solos e Engenharia Geotécnica. https://doi.org/10.4322/cobramseg.2022.0228.

Armelenti, G., Goldberg, K., Kuchle, J., De Ros, L.F., 2016. Deposition, diagenesis and reservoir potential of non-carbonate sedimentary rocks from the rift section of Campos Basin, Brazil. Pet. Geosci. 22, 1–17. https://doi.org/10.1144/petgeo2015-035.

Ashley, G.M., Renault, R.W., 2002. Rift sedimentation, vol. 73. SEPM Special Publication, pp. 3–7. https://doi.org/10.2110/pec.02.73.0003.

Asquith, G., Krygowski, D., 2004. Basic well log analysis: AAPG methods in exploration, vol. 16, pp. 37–76. https://doi.org/10.1306/Mth16823.

Awwiller, D.N., 1993. Illite/smectite formation and potassium transfer during burial diagenesis of mudrocks: A study from the Texas Gulf Coast Paleocene-Eocene. J. Sediment. Petrol. 63 (3), 501–512. https://doi.org/10.1306/D4267B3B-2B26-11D7-8648000102C1865D.

Balázs, A., Granjeon, D., Matenco, L., 2017. Tectonic and climatic controls on asymmetric half-graben sedimentation: Inferences from 3-D numerical modeling. Adv. Earth Space Sci. 36 (10), 2123–2141. https://doi.org/10.1002/2017TC004647.

Bassiouni, Z., 1994. Theory, measurement, and interpretation of well logs. In: SPE Textbook Series, 4, 372.

Bateman, R.M., 2020. Formation evaluation with pre-digital well logs. Elsevier, Amsterdam, Netherlands.

Bates, C.C., 1953. Rational theory of delta formation. Bull. Am. Assoc. Pet. Geol. 37 (9), 2119–2162. https://doi.org/10.1306/5CEADD76-16BB-11D7-8645000102C1865D.

Berner, R.A., 1984. Sedimentary pyrite formation: An update. Geochem. Cosmochim. Acta 48, 605–615. https://doi.org/10.1016/0016-7037(84)90089-9.

Bertetti, F.P., Prikryl, J.D., 2003. Mineralogy and geochemistry of well cuttings from selected early warning drilling project well in Fortymile wash. Center Nucl. Waste Regul. Analy. 76. San Antonio, Texas.

Bhuyan, K., Passey, Q.R., 1994. Clay estimation from GR and neutron-density porosity logs. SPWLA 35th Annual Logging Symposium. Tulsa, Oklahoma.

Boadu, F.K., Seabrook, B.C., 2006. Effects of clay content and salinity on the spectral electrical response of soils. J. Environ. Eng. Geophys. 11 (3), 161–170. https://doi.org/10.2113/JEEG11.3.161.

Bockris, J.O.'M., Reddy, A.K.N., Gamboa-Aldeco, M., 2000. In: Modern electrochemistry: Fundamentals of electrodics, second ed., 2A. Kluwer Academic Publishers.

Bond, L.J., Griffin, J.W., Denslow, K.M., Harris R.V., Jr., Schenkel, T., Persaud, A., Dale, G.E., Sood, A., Rutledge, J.T., Kovaleski, S., Keel, F., 2010. Nuclear source replacement in petrochemical well logging. Society of Exploration Geophysicists. https://doi.org/10.1190/1.3513833.

Boucot, A.J., Xu, C., Scotese, C.R., Morley, R.J., 2013. Phanerozoic paleoclimate: An atlas of lithologic indicators of climate. In: Concepts in Sedimentology and Paleontology, vol. 11. Society for Sedimentary Geology, p. 478. https://doi.org/10.2110/sepmcsp.11.

Bourgoyne, A.J.T., Chenevert, M.E., Millheim, K.K., 1986. Applied Drilling Engineering, Society of Petroleum Engineers, vol. 2. SPE Textbook Series.

Brekke, H., MacEachern, J.A., Roenitz, T., Dashtgard, S.E., 2017. The use of microresistivity image logs for facies interpretations: An example in point-bar deposits of the McMurray formation, Alberta, Canada. AAPG Bull. 101 (5), 655–682. https://doi.org/10.1306/08241616014.

Brigatti, M.F., Guidotti, C.V., Malferrari, D., Sassi, F.P., 2008. Single-crystal X-ray studies of trioctahedral mica coexisting with dioctahedral mica in metamorphic sequences from western Maine. Am. Mineral. 93 (2–3), 396–408. https://doi.org/10.2138/am.2008.2523.

Brindley, G.W., Brown, G., 1980. In: Quantitative X-ray mineral analysis of clays. Crystal structures of clay minerals and their X-ray identification, 5, pp. 411–438. https://doi.org/10.1180/mono-5.7.

Brunskill, G.J., 1969. Fayetteville Green Lake, New York. II. Precipitation and sedimentation of calcite in a meromictic lake with laminated sediments. Limnol. Oceanogr. 14, 830–847. https://doi.org/10.4319/lo.1969.14.6.0830.

Burley, S.D., 1993. Model of burial diagenesis for deep exploration plays in Jurassic fault traps of the Central and Northern North Sea. Geol. Soci. London, Petrol. Geol. Conf. Series. 4, 1353–1375. https://doi.org/10.1144/0041353.

Calabrese, A., Davis, H.C., 1970. Tolerances and Requirements of Embryos and Larvae of Bivalve Molluscs: Helgoländer Meeresuntersuchungen, vol. 20, pp. 553–564.

Calvo, J.P., Pozo, M., 2015. Geology of magnesian clays in sedimentary and non-sedimentary environments. In: Pozo, M., Galán, E. (Eds.), Magnesian Clays: Characterization, Origin and Applications. AIPEA Educational Series, Pub. No. 2. Digilabs, Bari, Italy, Madri Basin (Spain), pp. 123–174.

Carlotto, M.A., Silva, R.C.B., Yamato, A.A., Trindade, W.L., Moreira, J.L.P., Fernandes, R.A.R., Ribeiro, O.J.S., 2017. Libra: a newborn giant in the Brazilian pre-salt province. In: Merrill, R.K., Sternbach, C.A. (Eds.), Giant Fields of the Decade 2000–2010, 113. American Association of Petroleum Geologists, Memoir, pp. 165–176. https://doi.org/10.1306/13572006M1133685.

Carr, R., Yarbrough, L., Lentz, N., 2014. In: On-site XRF analysis of drill cuttings in the Williston Basin. Unconventional Resources Technology Conference Denver. USA. https://doi.org/10.15530/urtec-2014-1934308.

Carrado, K.A., Decarreau, A., Petit, S., Bergaya, F., Lagaly, G., 2006. Synthetic clay minerals and purification of natural clays. In: Bergaya, F., Lagaly, G. (Eds.), Handbook of Clay Science. Developments in Clay Science, vol. 1. Elsevier, pp. 115–139. https://doi.org/10.1016/S1572-4352(05)01004-4.

Carrasquilla, A., Lima, R., 2020. Basic and specialized geophysical well logs to characterize an offshore carbonate reservoir in the Campos Basin, southeast Brazil. J. S. Am. Earth Sci. 98, 102436. https://doi.org/10.1016/j.jsames.2019.102436.

Carroll, A.R., Bohacs, K.M., 1999. Stratigraphicclassification of ancient lakes: Balancing tectonic and climatic control. Geology 27, 99–102. https://doi.org/10.1130/0091-7613(1999)027<0099:SCOALB>2.3.CO;2.

Carugo, C., Malossi, A., Balossino, P., Galimberti, L., Gioacchini, F., Pingitore, F., Previde-Massara, E., Rivolta, F., 2013. Advanced cuttings analysis improves reservoir characterization and reduces operating times in shale gas drilling project. International Petroleum Technology Conference, Beijing. https://doi.org/10.2523/IPTC-17186-MS.

Carvalho, A.M.A., Hamon, Y., De Souza Jr, O.G., Carramal, N.G., Collard, N., 2022. Facies and diagenesis distribution in an Aptian pre-salt carbonate reservoir of the Santos Basin, Offshore Brazil: A comprehensive quantitative approach, 141, p. 105708. https://doi.org/10.1016/j.marpetgeo.2022.105708.

Cerling, T.E., 1994. Chemistry of closed basin lake waters: A comparison between African Rift Valley and some central North American rivers and lakes. In: Gierlowski-Kordesch, E., Kelts, K. (Eds.), Global Geological Record of Lake Basins. Cambridge University Press, pp. 29–30.

Chaaya, R., Gaboreau, S., Milet, F., Maubec, N., Tremosa, J., Raimbourg, H., Ferrage, E., 2023. In-operando X-ray scattering characterization of smectite swelling experiments. Appl. Clay Sci. 245. https://doi.org/10.1016/j.clay.2023.107124.

Chase, J.E., Arizaleta, M.L., Tutolo, B.M., 2021. A series of data-driven hypotheses for inferring biogeochemical conditions in alkaline lakes and their deposits based on the behavior of Mg and $SiO_2$. Minerals. https://doi.org/10.3390/min11020106.

Cheary, R.W., Coelho, A., 1992. A fundamental parameters approach to X-ray line-profile fitting. J. Appl. Crystallogr. 25 (2), 109–112. https://doi.org/10.1107/S0021889891010804.

Chinelatto, G.F., Belila, A.M.P., Basso, M., Souza, J.P.P., Vidal, A.C., 2020. A taphofacies interpretation of shell concentrations and their relationship with petrophysics: A case study of Barremian-Aptian coquinas in the Itapema Formation, Santos Basin-Brazil. Mar. Petrol. Geol. 116. https://doi.org/10.1016/j.marpetgeo.2020.104317.

Chumakov, N.M., Zharkov, M.A., Herman, A.B., Doludenko, M.P., Kalandadze, N.N., Lebedev, E.L., Ponomarenko, A.G., Rautian, A.S., 1995. Climatic belts of the mid-cretaceous time. Stratigr. Geol. Correl. 3 (3), 42–63.

Clavier, C., Coates, G., Dumanoir, J., 1984. Theoretical and experimental bases for the dual-water model for interpretation of Shaly sands. Soc. Petrol. Eng. J. 24 (2), 153–168. https://doi.org/10.2118/6859-PA.

Cohen, A.S., 2003. Paleolimnology: The history and evolution of lake systems. Oxford University Press. Oxford University Press, p. 525.

Coimbra, R., Rocha, F., Immenhauser, A., Olóriz, F., Terroso, D., Horikx, M., 2021. Carbonate-hosted clay minerals: A critical re-evaluation of extraction methods and their possible bias on paleoenvironmental information. Earth Sci. Rev., 103502 https://doi.org/10.1016/j.earscirev.2021.103502.

Conceição, J.C.J., Zalan, P.V., Wolff, S., 1988. Mecanismo, evolução e cronologia do rifte Sul-Atlântico. Bol. Geociências Petrobras 2, 255–265.

Corella, J., Brauer, A., Mangili, C., Rull, V., Vegas-Vilarrúbia, T., Morellón, M., Valero-Garcés, B., 2012. The 1.5-ka varved record of Lake Montcortès (Southern Pyrenees, NE Spain). Quat. Res. 78, 323–332. https://doi.org/10.1016/j.yqres.2012.06.002.

Craigie, N.W., 2015. Applications of chemostratigraphy in cretaceous sediments encountered in the North Central Rub's al-Khali Basin, Saudi Arabia. J. Afr. Earth Sci. 104, 27–42. https://doi.org/10.1016/j.jafrearsci.2015.01.003.

Craigie, N.W., 2018. Principles of Elemental Chemostratigraphy–A Practical User Guide. Springer, p. 189p.

Cupertino, D.F., Ramnani, C.W., Vanden Berg, M.D., Awramik, S.M., 2023. Formation of magnesium-clay in a lacustrine microbialite-bearing carbonate deposit, Eocene Green River Formation, Sanpete County, Utah. Sedimentology 71, 263–292. https://doi.org/10.1111/sed.13136.

Curtis, C.D., 1980. Diagenetic alteration in black shales. J. Geol. Soc. Lond. 137, 189–194. https://doi.org/10.1144/gsjgs.137.2.0189.

Curtis, C.D., 1995. Post-depositional evolution of mudstones: Early days and parental influences. J. Geol. Soc. Lond. 152, 577–586. https://doi.org/10.1144/gsjgs.152.4.0577.

Darragi, F., Tardy, Y., 1987. Authigenic trioctahedral smectites controlling pH, alkalinity, silica and magnesium concentrations in alkaline lakes. Chem. Geol. 63 (1–2), 59–72. https://doi.org/10.1016/0009-2541(87)90074-X.

Davies, S.J., Lamb, H.F., Roberts, S.J., 2015. Micro-XRF core scanning in palaeolimnology: Recent developments. Chapter 7. In: Croudace, I.W., Rothwell, R.G. (Eds.), Micro-XRF Studies of Sediment Cores–Applications of a Non-destructive Tool for the Environmental Sciences. Developments in Paleoenvironmental Research, vol. 17. Springer. Dordrecht. https://doi.org/10.1007/978-94-017-9849-5_72015.

Day-Stirrat, R.J., McDonnell, A., Wood, L.J., 2010. Diagenetic and seismic concerns associated with interpretation of deeply buried mobile shales. In: Wood, L. (Ed.), Shale Tectonics: AAPG Memoir, vol. 93, pp. 5–27. https://doi.org/10.1306/13231306M93730.

De Oliveira, F.V., Carmo de, I.O., Costa, J., Bittencourt, B.T., Lupinacci, W.M., Freire, A.F.M., 2024. Characterization of subaerial lava flows of the pre-salt strata in the Santos Basin based on basic well logs. J. S. Am. Earth Sci. 139. https://doi.org/10.1016/j.jsames.2024.104884.

Deocampo, D.M., 2015. Authigenic clay minerals in lacustrine mudstones. Geolog. Soci. Am. 515, 49–64. https://doi.org/10.1130/2015.2515(03.

de Wet, C.B., Godfrey, L., de Wet, A.P., 2015. Sedimentology and stable isotopes from a lacustrine-to-palustrine limestone deposited in an arid setting, climatic and tectonic factors: Miocene-Pliocene Opache Formation, Atacama Desert, Chile. Palaeogeogr. Palaeoclimatol. Palaeoecol. 426, 46–67. https://doi.org/10.1016/j.palaeo.2015.02.039.

Demicco, R.V., Hardie, L.A., 1994. Sedimentary structures and early diagenetic features of shallow marine carbonate deposits. SEPM (Society of Sedimentary Geology) 265. https://doi.org/10.2110/sepmatl.01.

Dias, J.F., 2005. Tectônica, estratigrafia e sedimentação no Andar Aptiano da margem leste brasileira. B. Geociências Petrobras 13 (1), 7–25.

Dunham, R.J., 1962. Classification of carbonate rocks according to depositional texture. In: Ham, W.E. (Ed.), Classification of Carbonate Rocks, vol. 1. American Association of Petroleum Geologists, pp. 108–121.

Ellis, D.V., Singer, J.M., 2007. Well logging for Earth scientists. Springer, Dodrecht. The Netherlands.

Embry, A.F., Klovan, J.E., 1971. A late Devonian reef tract on Northeastern Banks Island, NWT. Canad. Petrol. Geol. Bullet. 19, 730–781.

Flügel, E., 2004. Microfacies of carbonate rocks. Analysis, Interpretation and Application. Springer-Verlag, Berlin, Heidelberg, New York, p. 976.

Folk, R.L., 1968. Petrology of sedimentary rocks. Hemphill Publishing Co., Austin.

Föllmi, K.B., 2012. Early Cretaceous life, climate and anoxia. Cretac. Res. 35, 230–257. https://doi.org/10.1016/j.cretres.2011.12.005.

França, D., Bobco, F.E.R., Lupinacci, W.M., Freire, A.F.M., 2023. Simple approach to sediment washing for drill cuttings description of pre-salt rocks. XVI Latin American Congress on Organic Geochemistry. Poster. Aracaju. Brazil.

Freed, R.L., Peacor, D.R., 1989. Variability in temperature of the smectite/illite reaction in Gulf Coast sediments. Clay Miner. 24, 171–180. https://doi.org/10.1180/claymin.1989.024.2.05.

Freitas de, V.A., Vital, J.C., Rodrigues, B.R., Rodrigues, R., 2022. Source rock potential, main depocenters and $CO_2$ occurrence in the pre-salt section of Santos Basin, southeast Brazil. J. S. Am. Earth Sci. 115. https://doi.org/10.1016/j.jsames.2022.103760.

Friedman, G., Sanders, J.E., Kopaska-Merkel, D.C., 1992. Principles of sedimentary deposits, Stratigraphy and Sedimentology. Macmillan, New York, p. 717.

Frostick, L., Reid, I., 1989. Is structure the main control of river drainage and sedimentation in rifts? J. Afr. Earth Sci. 8, 165–182. https://doi.org/10.1016/S0899-5362(89)80022-3.

Frostick, L., Reid, I., 1990. Structural control of sedimentation patterns and implication for the economic potential of the East African Rift basins. J. Afr. Earth Sci. 10, 307–318. https://doi.org/10.1016/0899-5362(90)90062-J.

Fu, S., Liu, Z., Zhang, Y.M., Wang, X., Tian, N., Yao, N., Xiong, Y., Chen, P., Li, L., Wang, H.L., 2019. Depositional systems and sequence stratigraphy of Mesozoic lacustrine rift basins in NE China: A case study of the Wulan-Hua sag in the southern Erlian Basin. J. Asian Earth Sci. 174, 68–98. https://doi.org/10.1016/j.jseaes.2018.11.020.

Galán, E., Pozo, M., 2011. Palygorskite and sepiolite deposits in continental environments. Description, genetic patterns and sedimentary settings. In: Galán, E., Singer, A. (Eds.), Developments in Clay Science. Elsevier B.V, Amsterdam, pp. 125–173. https://doi.org/10.1016/B978-0-444-53607-5.00006-2.

Garrouch, A.A., Sharma, M.M., 1994. The influence of clay content, salinity, stress and wettability on the electrical properties of brine saturated rocks: 10 Hz to 10 MHz. Geophysics 59, 909–917. https://doi.org/10.1190/1.1443650.

Gawthorpe, R.L., Hardy, S., Ritchie, B., 2003. Numerical modelling of depositional sequences in half-graben rift basins. Sedimentology 50 (1), 169–185. https://doi.org/10.1046/j.1365-3091.2003.00543.x.

Gawthorpe, R.L., Leeder, M.R., 2000. Tectono-sedimentary evolution of active extensional basins. Basin Res. 12 (3–4), 195–218. https://doi.org/10.1111/j.1365-2117.2000.00121.x.

Glenn, C.R., Kelts, K., 1991. Sedimentary rhythms in Lake deposits. In: Cycles and Events in Stratigraphy. Springer. Verlag.

Glover, P.W.J., Meredith, P.G., Sammonds, P.R., Murrel, S.A.F., 1994. Ionic surface conductivity in sandstone. J. Geophys. Res. 99, 21635–21650.

Goldberg, K., Kuchle, J., Scherer, C., Alvarenga, R., Ene, P.L., Armelenti, G., De Ros, L.F., 2017. Re-sedimented deposits in the rift section of the Campos Basin. Mar. Petrol. Geol. 80, 412–431.

Gomes, J.P.B., Bunevich, R.B., Tonietto, S.N., Alves, D.B., Santos, J.F., Whitaker, F.F., 2020. Climatic signals in lacustrine deposits of the Upper Yacoraite Formation, Western Argentina: Evidence from clays minerals, analcime, dolomite and fibrous calcite. Sedimentology 67, 2282–2309. https://doi.org/10.1111/sed.12700.

Gonzaga, H.M., Novo, T.A., Silva da, J.T.G., Fonte Boa, T.M.R., Gonçalves, L.C., Cordeiro, M.S., 2024. Stratigraphy and drilling geomechanics of a thick salt section: The Ariri formation in the eastern portion of the Santos Basin. J. S. Am. Earth Sci. 135. https://doi.org/10.1016/j.jsames.2024.104802.

Gunderson, R., Cumming, W., Astra, D., Harvey, C., 2000. Analysis of smectite clays in geothermal drill cuttings by methylene blue method: For well site geothermometry and resistivity sounding correlation. In: Proceedings World Geothermal Congress. Tohoku, Japan.

Harris, N.M., Freeman, K.H., Pancost, R.D., White, T.S., Mitchell, G.D., 2004. The character and origin of syn-rift lacustrine hydrocarbon source rocks of the Congo Basin, West Africa. AAPG Bull. 88, 1163–1184. https://doi.org/10.1306/02260403069.

Hay, W.W., Floegel, S., 2013. New thoughts about the Cretaceous climate and oceans. Earth Sci. Rev. 115, 262–272. https://doi.org/10.1016/j.earscirev.2012.09.008.

He, J., Croix, A.D.L., Wang, J., Ding, W., Underschultz, J.R., 2019. Using neural networks and the Markov Chain approach for facies analysis and prediction from well logs in the Precipice Sandstone and evergreen Formation, Surat Basin, Australia. Mar. Petrol. Geol. 101, 410–427. https://doi.org/10.1016/j.marpetgeo.2018.12.022.

Heimhofer, U., Ariztegui, D., Lenniger, M., Hesselbo, S.P., Martill, D.M., 2010. High resolution multiproxy records from Early Cretaceous lacustrine deposits: The laminated Crato fossil beds of Brazil. Sedimentology 57, 677–694.
Herlinger, R., Zambonato, E., De Ros, L.F., 2017. Influence of diagenesis on the quality of Lower Cretaceous pre-salt Lacustrine Carbonate reservoirs from Northern Campos Basin, offshore Brazil. J. Sediment. Res. 87 (12), 1285–1313. https://doi.org/10.2110/jsr.2017.70.
Hesse, R., 1989. Silica diagenesis: Origin of inorganic and replacement cherts. Earth Sci. Rev. 26 (1–3), 253–284. https://doi.org/10.1016/0012-8252(89)90024-X.
Holmer, M., Storkholm, P., 2001. Sulphate reduction and sulphur cycling in lake sediments: A review. Freshw. Biol. 46, 431–451. https://doi.org/10.1046/j.1365-2427.2001.00687.x.
Hou, Y., Wang, H., Fan, T., Zhang, H., Yang, R., Li, Y., Long, S., 2020. Rift-related sedimentary evolution and its response to tectonics and climate changes: A case study of the Guaizihu sag, Yingen-Ejinaqi Basin, China. J. Asian Earth Sci. 195. https://doi.org/10.1016/j.jseaes.2020.104370.
Ilgara, A., Nemec, W., 2005. Early Miocene lacustrine deposits and sequence stratigraphy of the Ermenek Basin, Central Taurides, Turkey. Sediment. Geol. 173 (1–4), 233–275. https://doi.org/10.1016/j.sedgeo.2003.07.007.
Imbuzeiro, B.M., Vidal, F., da Rocha de, B.S.N., Silveira, C.S., Lupinacci, W.M., Salgado-Campos, V., Freire, A.F.M., 2024. An integrated approach to characterize diabase sills in Parnaíba Basin, based on geochemical data, cuttings description, and well logs interpretation. J. S. Am. Earth Sci. https://doi.org/10.1016/j.jsames.2024.105263.
Ito, M., Matsukawa, M., Saito, T., Nichols, D.J., 2006. Facies architecture and paleo hydrology of a synrift succession in the Early Cretaceous Choyr Basin, south eastern Mongolia. Cretac. Res. 27, 226–240. https://doi.org/10.1016/j.cretres.2005.11.005.
Jackson, M.L., 1975. In: Soil Chemical Analysis: Advanced Course, second ed. Parallel Press, Madison.
Jewuła, K., Trela, W., Wasielka, N., Archer, S.G., 2023. Palustrine limestones and calcretes as the sedimentary record of paleoenvironmental changes in a late Permian semi-arid climate at the SE periphery of the Southern Permin Basin (the Holy Cross Mountains, Poland). Palaeogeogr. Palaeoclimatol. Palaeoecol. 614. https://doi.org/10.1016/j.palaeo.2023.111398.
Johnson, T.C., Odada, E.O., 1996. The limnology, climatology and paleoclimatology of the East African lakes. Gordon & Breach, Amsterdam, p. 664.
Jones, B.F., 1986. Clay mineral diagenesis in lacustrine sediments. US Geol. Surv. Bull. 1578, 291–300. https://doi.org/10.3133/b1578.
Kämpf, L., Brauer, A., Dulski, P., Lami, A., Marchetto, A., Gerli, S., Ambrosetti, W., Guilizzoni, P., 2012. Detrital layers marking flood events in recent sediments of Lago Maggiore (N. Italy) and their comparision with instrumental data. Freshw. Biol. 57, 2076–2090. https://doi.org/10.1111/j.1365-2427.2012.02796.x.
Katz, B.J., 1953. Lacustrine Basin exploration: Case studies and modern analogs, pp. 340. American Association of Petroleum Geologists.
Keeton, G., Pranter, M., Cole, R.D., Gustason, E.R., 2015. Stratigraphic architecture of fluvial deposits from borehole images, spectral-gamma-ray response, and outcrop analogs, Piceance Basin, Colorado. AAPG Bull. 99 (10), 1929–1956.
Kern, A., Eysel, W., 1993. Mineralogisch-Petrograph. Institute, University of Hidelberg, Germany. ICDD Grant-in-Aid.
KGS – Kansas Geological Survey, 2017. Reading Lithology from a Neutron-Density Porosity Log Overlay. https://www.kgs.ku.edu/Publications/Bulletins/LA/05_overlay.html. (Accessed 24 January 2025)
Kidwell, S.M., Bosence, D.W.J., 1991. Taphonomy and time-averaging of marine shelly faunas. In: Allison, P.A., Briggs, D.E. (Eds.), Taphonomy, Releasing the Data Locked in the Fossil Record: Topics in Geobiology, pp. 115–209.
Kowalska, S., Kubik, B., Skupio, R., Wolanski, K., 2020. Downhole lithological profile reconstruction based on chemical composition of core samples and drill Cuttings measured with portable X-ray fluorescence spectrometer. Minerals 10, 1101. https://doi.org/10.3390/min10121101.
Kreuser, T., 1995. Tectonic and climatic controls of lacustrine sedimentation in pre-rift and rift settings in the Permian-Triassic of East Africa. J. Paleolimnol. 13 (1), 3–19. https://doi.org/10.1007/bf00678108.
Lai, J., Su, Y., Xiao, L., Zhao, F., Bai, T., Li, H., Huang, Y., Wang, G., Qin, Z., 2024. Application of geophysical well logs in solving geologic issues: Past, present and future prospect. Geosci. Front. 15. https://doi.org/10.1016/j.gsf.2024.101779.
Lai, J., Wang, G., Fan, Q., Zhao, F., Zhao, X., Li, Y., Zhao, Y., Pang, X., 2023. Towards the scientific interpretation of geophysical well logs: Typical misunderstandings and countermeasures. Surv. Geophys. 44, 463–494.
Lambiase, J., 1990. A model for tectonic control of lacustrine stratigraphic sequences in continental rift basins. AAPG Memoir 50, 265–276. https://doi.org/10.1306/m50523c16.
Lapeyrouse, N.J., 2002. Formulas and calculations for drilling, production and workover. Gulf Professional publishing, Boston, p. 381.
Lauterbach, S., Brauer, A., Andersen, N., Danielopol, D., Dulski, P., Hüls, M., Milecka, K., Namiotko, T., Obremska, M., Grafenstein, U., Participants, D., 2011. Environmental responses to Lateglacial climatic fluctuations recorded in the sediments of pre-alpine Lake Mondsee (northeastern Alps). J. Quat. Sci. 26, 253–267. https://doi.org/10.1002/jqs.1448.
Leeder, M.R., Gawthorpe, R.L., 1987. Sedimentary models for extensional tilt-block/half-graben basins. Geol. Soc. London Special Publ. 28 (1), 139–152. https://doi.org/10.1144/GSL.SP.1987.028.01.
Leite de, C.O.N., Assis Silva de, C.M., De Ros, L.F., 2020. Depositional and diagenetic processes in the pre-salt rift section of a Santos Basin area, SE Brazil. J. Sediment. Res. 90, 584–608. https://doi.org/10.2110/jsr.2020.27.
Leon de, J.A.L., Penteado de, H.L.B., Ellis, G.S., Milkov, A., Filho, J.G.M., 2024. Recognition of artificial gases formed during drill-bit metamorphism using advanced mud gas. Energies 17, 4383. https://doi.org/10.3390/en17174383.
Leppard, C.W., Gawthorpe, R.L., 2006. Sedimentology of rift climax deep water systems; Lower Rudeis Formation, Hammam Faraun fault block, Suez Rift, Egypt. Sediment. Geol. 191 (1), 67–87. https://doi.org/10.1016/j.sedgeo.2006.01.006.
Lerman, A., 1978. Lakes, Chemistry, Geology, Physics. Springer-Verlag Berlin Heidelberg, p. 368.
Li, G., Zhang, H., Liu, X., Yang, H., Wang, X., Zhang, X., Jonell, T.N., Zhang, Y., Huang, X., Wang, Z., Yixuan, W., Yu, L., Xia, D., 2020. Paleoclimatic changes and modulation of East Asian summer monsoon by high-latitude forcing over the last 130,000 years as revealed by independently dated loess-paleosol sequences on the NE Tibetan Plateau. Quat. Sci. Rev. 237, 106283. https://doi.org/10.1016/j.quascirev.2020.106283.
Lima, B.E.M., De Ros, L.F., 2019. Deposition, diagenetic and hydrothermal processes in the Aptian Pre-Salt lacustrine carbonate reservoirs of the northern Campos Basin, offshore Brazil. Sediment. Geol. 383, 55–81. https://doi.org/10.1016/j.sedgeo.2019.01.006.
Lin, C., Eriksson, K., Li, S., Wan, Y., Ren, J., Zhang, Y., 2001. Sequence architecture, depositional systems, and controls on development of lacustrine basin fills in part of the Erlian Basin, northeast China. AAPG Bull. 85 (11), 268–269.
Lipson, H., Stokes, A.R., 1942. The structure of graphite. In: Proceedings of the Royal Society A: Mathematical, Physical and Engineering Sciences, vol. 181, pp. 101–105. https://doi.org/10.1098/rspa.1942.0063.
Liu, C.R., 2017. Theory of electromagnetic well logging. Elsevier.
Locke, A., 2008. Tabulated observations of the pH tolerance of marine and estuarine biota: Fisheries and Oceans Canada, pp. 1–28.
Luthi, S., 2001. Geological Well Logs: Their use in reservoir modelling. Springer-Verlag, Berlin Heidelberg New York.
Marshall, M.H., Lamb, H.F., Huws, D., Davies, S.J., Bates, C.R., Bloemendahl, J., Boyle, J.F., Leng, M.J., Umer, M., Bryant, C.L., 2011. Lete Pleistocene and Holocene drought events at Lake Tana, the source of the Blue Nile. Global Planet. Change 78, 147–161. https://doi.org/10.1016/j.glopacha.2011.06.004.
Martins-Neto, M.A., 2000. Tectonics and sedimentation in a paleo/mesoproterozoic rift-sag basin (Espinhaço Basin, southeastern Brazil). Precambr. Res. 103 (3), 147–173. https://doi.org/10.1016/s0301-9268(00)00080-2.
Maynard, J.B., 1984. Composition of plagioclase feldspar in modern deep-sea sands: Relationship to tectonic setting. Sedimentology 31, 493–501.
McKinley, J.M., Worden, R.H., Ruffell, A.H., 1999. Smectite in sandstones: A review of the controls on occurrence and behavior during diagenesis. Clay Miner. Cem. Sandstones 109–128. https://doi.org/10.1002/9781444304336.ch5.
Mendes, M.M., Paulo, M., Reolid, M., 2023. The upper Hauterivian–Barremian (Lower Cretaceous) Arrifes section (Algarve Basin, Southern Portugal): A palynostratigraphic and palaeoenvironmental approach. Cretac. Res. 146, 105433. https://doi.org/10.1016/j.cretres.2022.105433.
Milani, E.J., Brandão, J.A.S.L., Zalán, P.V., Gamboa, L.A.P., 2000. Petróleo na margem continental brasileira: Geologia, exploração, resultados e perspectivas. Rev. Bras. Geofís. 18 (3). https://doi.org/10.1590/S0102-261X2000000300012.
Milani, E.J., Rangel, H.D., Bueno, G.V., Stica, J.M., Winter, W.R., Caixeta, J.M., Neto, O.C.P., 2007. Bacias sedimentares Brasileiras, cartas estratigráficas. Bol. Geociencias Petrobras 15, 183–205.
Milliken, K.L., 2003. Late diagenesis and mass transfer in sandstone-shale sequences. Treat. Geochem. 7, 159–190. https://doi.org/10.1016/B0-08-043751-6/07091-2.
Milliken, K.L., 1989. Petrography and composition of authigenic feldspar, Oligocene Frio Formation, South Texas. J. Sediment. Petrol. 59, 361–374. https://doi.org/10.1306/212F8F94-2B24-11D7-8648000102C1865D.
Milliken, K.L., Ergene, S.M., Ozkan, A., 2016. Quartz types, authigenic and detrital, in the Upper Cretaceous Eagle Ford Formation, South Texas, USA. Sediment. Geol. 339, 273–288. https://doi.org/10.1016/j.sedgeo.2016.03.012.
Milliken, K.L., Reed, R.M., McCarty, D.K., Bishop, J., Lipinski, C.J., Fischer, T.B., Crousse, L., Reijenstein, H., 2019. Grain assemblages and diagenesis in the Vaca Muerta Formation (Jurassic-Cretaceous), Neuquén Basin, Argentina. Sedim. Geol. 380, 45–64. https://doi.org/10.1016/j.sedgeo.2018.11.007.
Milliken, K.L., 1988. Loss of provenance information through subsurface diagenesis in Plio-Pleistocene sandstones, Gulf of Mexico. J. Sediment. Petrol. 58, 992–1002. https://doi.org/10.1306/212F8EE0-2B24-11D7-8648000102C1865D.
Milliken, K.L., 1992. Chemical behavior of detrital feldspar in mudrocks versus sandstones, Frio Formation (Oligocene), South Texas. J. Sediment. Petrol. 62, 790–801. https://doi.org/10.1306/D42679DD-2B26-11D7-8648000102C1865D.
Mitchell, R.F., Miska, S., Aadny, B.S., 2011. Fundamentals of drilling engineering. Society of Petroleum Engineers, Richardson, TX, p. 696.
Mizusaki, A.M.P., Petrini, R., Bellieni, G., Comin-Chiaramonti, P., Dias, J., De Min, A., Piccirillo, E.M., 1992. Basalt magmatism along the passive continental margin of SE Brazil (Campos Basin). Contrib. Mineral. Petrol. 111, 143–160.
Moore, D.M., Reynolds, R.C., 1997. X-ray diffraction and the identification and analysis of clay minerals. Oxford University Press, Oxford, p. 392.
Morad, S., 1998. Carbonate cementation in sandstones: Distribution patterns and geochemical evolution. In: Morad, S. (Ed.), Carbonate Cementation in Sandstones, vol. 26. International Association of Sedimentologists, Special Publications, pp. 1–26.

Moreira, J.L.P., Madeira, C.V., Gil, J.A., Machado, M.A.P., 2007. Bacia de Santos. Bol. Geociencias Petrobras 15 (2), 531–549.

Morley, C.K., Nelson, R.A., Patton, T.L., Munn, S.G., 1990. Transfer zones in the east African Rift system and their relevance to hydrocarbon exploration in rifts. AAPG Bull. 74, 1234–1253. https://doi.org/10.1306/0C9B2475-1710-11D7-8645000102C1865D.

Moulin, M., Aslanian, D., Unternehr, P., 2005. Geological constraints on the evolution of the Angolan margin based on reflection and refraction seismic data (ZaïAngo project). Geophys. J. Int. 162 (3), 793–810. https://doi.org/10.1111/j.1365-246X.2005.02668.x.

Mulder, T., Alexander, J., 2001. The physical character of subaqueous sedimentary density flows and their deposits. Sedimentology 48, 269–299.

Muniz, M.C., 2014. Tectono-stratigraphic evolution of the Barremian–Aptian continental rift carbonates in southern Campos Basin, Brazil. Royal Holloway University of London, p. 324.

Nabawy, B.S., Géraud, Y., 2016. Impacts of pore- and petro-fabrics, mineral composition and diagenetic history on the bulk thermal conductivity of sandstones. J. Afr. Earth Sci. 115, 48–62.

Nery, G.G., 2005. Perfilagem Geofísica (Relatório de Pesquisa/2005). Hydrolog Serviços de Perfilagens LTDA. Salvador. BA.

Olatinsu, O.B., Olorode, D.O., Clennell, B., Esteban, L., Josh, M., 2017. Lithotype characterizations by nuclear magnetic resonance (NMR): A case study on limestone and associated rocks from the Eastern Dahomey Basin, Nigeria. J. Afr. Earth Sci. 129, 701–712. https://doi.org/10.1016/j.jafrearsci.2017.02.005.

Olhoeft, G.R., 1981. Electrical properties of rocks. In: Touloukian, Y.S., Judd, Y.S., Roy, R.F. (Eds.), Physical Properties of Rocks and Minerals. McGraw-Hill, 1981.

Olsen, P.E., 1986. A 40-million-year lake record of early Mesozoic orbital climatic forcing. Science 234, 842–848. https://doi.org/10.1126/science.234.4778.84.

Olsen, P.E., 1990. Tectonic, climatic, and biotic modulation of lacustrine ecosystems: Examples from newark supergroup of eastern North America, vol. 50. AAPG Mem, pp. 209–224.

Osório-Sanabria, L.L., 2022. Geoquímica orgânica e isotópica das formações: Piçarras, Itapema e Barra Velha no campo de Lula, Bacia de Santos. Tese de Doutorado. Universidade do Estado do Rio de Janeiro, Rio de Janeiro. pp. 233.

Pedrinha, S., Artagão de, V.M., 2024. High-resolution stratigraphy and characterization of reservoir-critical heterogeneities in the Giant Tupi Field, Presalt Santos Basin, Brazil. Geological Society, London, Special Publications, p. 548.

Peltonen, C., Marcussen, Ø., Bjørlykke, K., Jahren, J., 2009. Clay mineral diagenesis and quartz cementation in mudstones: The effects of smectite to illite reaction on rock properties. Mar. Petrol. Geol. 6, 887–898. https://doi.org/10.1016/j.marpetgeo.2008.01.021.

Peretomode, E., Oluyemi, G., Faisal, N.H., 2022. Oilfield Chemical-formation interaction and the effects on petrophysical properties: A review. Arabian J. Geosci. 15, 1223. https://doi.org/10.1007/s12517-022-10469-9.

Pietzsch, R., Oliveira, D.M., Tedeschi, L.R., Queiroz Neto, J.V., Figueiredo, M.F., Vazquez, J.C., de Souza, R.S., 2018. Palaeohydrology of the Lower Cretaceous pre-salt lacustrine system, from rift to post-rift phase, Santos Basin, Brazil. Palaeogeogr. Palaeoclimatol. Palaeoecol. 507, 60–80. https://doi.org/10.1016/j.palaeo.2018.06.043.

Platt, N.H., Wright, V.P., 1991. Lacustrine carbonates: facies models, facies distributions and hydrocarbon aspects. In: Anadón, P., Cabrera, L.I., Kelts, K. (Eds.), Lacustrine Facies Analysis, vol. 13. Special Publication, International Association of Sedimentologists, pp. 55–73.

Potter, P.E., Maynard, J.B., Depetris, P.J., 2005. Mud and Mudstones – Introduction and Overview. University of Cincinnati, Ohio, USA, p. 304. https://doi.org/10.1029/2005EO140006.

Pozo, M., Casas, J., 1999. Origin of Kerolite and associated Mg clays in palustrine–lacustrine environments: The Esquivias deposit (Neogene Madrid Basin, Spain). Clay Miner. 34, 395–418.

Pozo, M., Calvo, J., 2018. An overview of authigenic magnesian clays. Minerals. https://doi.org/10.3390/min8110520.

Pozo, M., Galán, E., 2015. Magnesian clays – characterization, origin and applications (pub. no. 2). AIPEA Educ. Ser. (Italy), 397.

Prosser, S., 1993. Rift-related linked depositional systems and their seismic expression. Geol. Soc. London Special Publ. 71 (1), 35–66. https://doi.org/10.1144/GSL.SP.1993.071.01.03.

Qi, Y., Wu, Y., 2022. Electrical conductivity of clayed rocks and soils: A non-linear model. Geophys. Res. Lett. 49. https://doi.org/10.1029/2021GL097408 e2021GL097408.

Qin, Y., Zhu, X., Zhu, S., McElroy, B., 2021. Impact of deep-time palaeoclimate on the sedimentary records and morphology of lacustrine shoal-water deltas, Upper Eocene Dongying depression, Bohai Bay Basin, China. Sedimentology 68 (7), 3253–3278.

Raiswell, R., 1982. Pyrite texture, isotopic composition and the availability of iron. Am. J. Sci. 82, 1244–1263.

Riccomini, C., Sant'anna, L.G., Tassinari, C.C.G., 2012. Pré-sal: Geologia e exploração. Rev. USP 95, 33–42. https://doi.org/10.11606/issn.2316-9036.v0i95p33-42.

Rider, M.H., 2002. The geological interpretation of well logs. Interprint Ltd, Malta.

Rietveld, H., 1969. A profile refinement method for nuclear and magnetic structures. J. Appl. Crystallogr. 2, 65–71. https://doi.org/10.1107/S0021889869006558.

Rollinson, H., Pease, V., 2021. In: Using chemical data to understand geological processes, second ed. Cambridge University Press, p. 661. https://doi.org/10.1017/9781108777834.

Salgado-Campos, V.M.J., Carvalho, I.S., Bertolino, L.C., Duarte, T.A., Araújo, B.C., Borghi, L., 2021. Clay mineralogy and lithogeochemistry of lutites from the Lower Cretaceous Crato Member, Araripe Basin, NE Brazil: Implications for paleoenvironmental, paleoclimatic and provenance reconstructions. J. S. Am. Earth Sci. 110, 103329. https://doi.org/10.1016/j.jsames.2021.103329.

Salgado-Campos, V.M.J., Carvalho, I.S., Bertolino, L.C., Borghi, L., Rios-Netto, A.M., Araújo, B.C., Souza, D.C., Ferreira, L.O., Bobco, F.E., 2022. Unraveling an alkaline lake and a climate change in Northeastern Brazil during the Late Aptian. Sediment. Geol. 442. https://doi.org/10.1016/j.sedgeo.2022.106290.

Samanta, A., Bera, M.K., Sarkar, A., 2016. Climate-modulated sequence development in a tropical rift basin during the late Palaeocene to early Eocene super greenhouse Earth. Sedimentology 63 (4), 917–939.

Santos, H.N., Neumann, R., Ávilla, C.A., 2017. Mineral quantification with simultaneous refinement of Ca-Mg carbonates non-stoichiometry by X-ray diffraction, Rietveld method. Minerals 7 (9), 164. https://doi.org/10.3390/min7090164.

Sartorato, A.C., Tonietto, S., Pereira, E., 2020. Silicification and dissolution features in the brazilian pre-salt Barra Velha formation: Impacts in the reservoir quality and insights for 3D geological modeling. Rio Oil&Gas. https://doi.org/10.48072/2525-7579.rog.2020.068.

Schieber, J., Krinsley, D., Riciputi, L., 2000. Diagenetic origin of quartz silt in mudstones and implications for silica cycling. Nature 406, 972–985. https://doi.org/10.1038/35023143.

Scholz, C.A., Rosendahl, B.R., Scott, D.L., 1990. Development of coarse-grained facies in lacustrine rift basins: Examples from East Africa. Geology 18 (2), 140–144. https://doi.org/10.1130/0091-7613(1990)018<0140:DOCGFI>2.3.CO;2.

Segev, A., 2002. Flood basalts, continental breakup & the dispersal of Gondwana: Evidence for periodic migration of upwelling mantle flows (plumes). European Geosciences Union, Stephan Mueller, vol. 2. Special Publication, pp. 171–191. https://doi.org/10.5194/smsps-2-171-2002.

Shapiro, S.S., Wilk, M.B., 1965. An analysis of variance test for normality (complete samples). Biometrika 52 (3–4), 591–611. https://doi.org/10.1093/biomet/52.3-4.591.

Souza, L.S., Sgarbi, G.N.C., 2019. Bacia de Santos no Brasil: Geologia, exploração e produção de petróleo e gás natural. Bol. Geol. 41, 175–195. https://doi.org/10.18273/revbol.v41n1-2019009.

Spearman, C., 1904. The proof and measurement of association between two things. Am. J. Psichol/ 15, 72–101.

Stuckman, M.Y., Lopano, C.L., Berry, S.M., Hakala, J.A., 2019. Geochemical solid characterization of drill cuttings, core and drilling mud from marcellus shale energy development. J. Nat. Gas Sci. Eng. 68. https://doi.org/10.1016/j.jngse.2019.102922.

Surdam, R.C., Crossey, L.J., 1985. Organic–inorganic reactions during progressive burial: Key to porosity and permeability enhancement and preservation. Royal society of London, Philosophical transactions, Series A, Mathematical and Physical Sciences, 315, pp. 135–156. https://doi.org/10.1098/rsta.1985.0034.

Tan, M., Wang, P., Mao, K., 2014. Comparative study of inversion methods of three-dimensional NMR and sensitivity to fluids. J. Appl. Geophys. 103 (4), 12–30.

Taylor, K.G., 1998. Spatial and temporal variations in early diagenetic organic matter oxidation pathways in lower Jurassic mudstone of eastern England. Chem. Geol. 145, 47–60. https://doi.org/10.1016/S0009-2541(97)00119-8.

Taylor, K.G., Macquaker, J.H.S., 2018. Diagenetic alterations in a silt and clay rich mudstone succession: An example from the Upper Cretaceous Mancos Shale of Utah, USA. Clay Miner. 49, 213–227. https://doi.org/10.1180/claymin.2014.049.2.05.

Technisch Physiscge Dienst, 1966. ICDD Graint-in-Aid. Delft, The Netherlands.

Terra, G.J.S., Spadini, A.R., França, A.B., Leite, C.S., Zambonato, E.E., Juschhaks, L.C.S., Arienti, L.M., Erthal, M.M., Blauth, M., Franco, M.P., Matsuda, N.S., Silva, N.G.C., Junior, P.A.M., D'Avila, R.S.F., Souza, R.S., Tonietto, S.N., Anjos, S.M.C., Campinho, V.S., Winter, W.R., 2010. Carbonate rock classification applied to Brazilian sedimentary basins. Bol. Geociencias Petrobras 18, 9–29.

Thomas, R.L., Kemp, A.L.W., Lewis, C.F.M., 1972. Distribution composition and characteristics of the surficial sediments of Lake Ontario. J. Sediment. Petrol. 42, 66–84.

Thomas, R.L., Kemp, A.L.W., Lewis, C.F.M., 1973. The surficial sediments of Lake Huron. Can. J. Earth Sci. 10, 226–271. https://doi.org/10.1139/e73-023.

Thyberg, B., Jahren, J., Winje, T., Bjørlykk, K., Faleide, J.I., Marcussen, Ø., 2010. Quartz cementation in Late Cretaceous mudstones, northern North Sea: Changes in rock properties due to dissolution of smectite and precipitation of micro-quartz crystals. Mar. Petrol. Geol. 27 (8), 1752–1764. https://doi.org/10.1016/j.marpetgeo.2009.07.005.

Tiercelin, J.J., 1990. Rift-basin sedimentation: responses to climate, tectonism and volcanism. Examples of the East African Rift. J. Afr. Earth Sci. 10, 283–305. https://doi.org/10.1016/0899-5362(90)90061-I.

Tosca, N.J., 2015. Geochemical pathway to Mg-silicate formation. In: Pozo, M., Galán, E. (Eds.), Magnesian Clays: Characterization, Origin and Applications, 2. AIPEA Educational Series, pp. 283–329.

Tosca, N.J., Masterson, A.L., 2014. Chemical controls on incipient Mg-silicate crystallization at 25 °C: Implications for early and late diagenesis. Clay Miner. 49, 165–194. https://doi.org/10.1180/claymin.2014.049.2.03.

Towe, K.M., 1962. Clay mineral diagenesis as a possible source of silica cement in sedimentary rocks. J. Sediment. Petrol. 32, 26–28.

Tucker, T.E., Jones, S.J., 2023. In: Sedimentary Petrology, 4° Ed. Wiley, p. 426.

Tutolo, B.M., Tosca, N.J., 2018. Experimental examination of the mg-silicate-carbonate system at ambient temperature: Implications for alkaline chemical sedimentation and lacustrine carbonate formation. Geochem. Cosmochim. Acta 225, 80–101. https://doi.org/10.1016/j.gca.2018.01.019.

Verrecchia, E., 2008. Lacustrine and palustrine geochemical sediments. Geochemical Sediments and Landscapes, pp. 298–329. https://doi.org/10.1002/9780470712917.ch9.
Viani, A., Gualtieri, A.F., Artioli, G., 2002. The nature of disorder in montmorillonite by simulation of X-ray powder patterns. Am. Mineral. 87 (7), 966–975. https://doi.org/10.2138/am-2002-0720.
Vidal, F.C., Gomes, R.T.M., Roriz, C.E.D., Silva, K.M.S., Toledo, R.C., 2022. Lithology identification through X-Ray fluorescence (XRF): Analyses on drill cuttings while drilling. In: Santos Basin. SPE Annual Technical Conference and Exhibition. https://doi.org/10.2118/210151-MS. Houston, Texas, USA.
Vinegar, H.L., Waxman, M.H., 1984. Induced polarization of shaly sands. Geophysics 49, 1267–1287. https://doi.org/10.1190/1.1441755.
Vonhof, H.B., Joordens, J.C.A., Noback, M.L., Vand Der Lubbe, J.H.J.L., Feibel, C.S., Kroon, D., 2013. Environmental and climatic control on seasonal stable isotope variation of freshwater molluscan bivalves in the Turkana Basin (Kenya). Palaeogeogr. Palaeoclimatol. Palaeoecol. 383–384, 16–26. https://doi.org/10.1016/j.palaeo.2013.04.022.
Walker, D., Verma, P.K., Cranswick, L.M.D., Jones, R.L., Clark, S.M., Buhre, S., 2004. Halite-sylvite thermoelasticity Sample: msl416032, T = 100 C, P = 0.0 lbar, cell volume = 180.65 ang**3. Am. Mineral. 89, 204–210.
Wang, G.W., Lai, J., Liu, B.C., Fan, Z.Y., Liu, S.C., Shi, Y.J., Zhang, H.T., Chen, J., 2020. Fluid property discrimination in dolostone reservoirs using well logs. Acta Geol. Sin-Engl. 94 (3), 831–846.
Wang, L., Liu, B., Bai, L., Ma, L., Yu, Z., Huo, Q., Taylor, K.G., 2024. Differential mineral diagenetic evolution of lacustrine shale: Implications for $CO_2$ storage. Int. J. Coal Geol. 295. https://doi.org/10.1016/j.coal.2024.104629.
Warr, L.N., 2021. IMA–CNMNC approved mineral symbols. Mineral. Mag. 85 (3), 291–320. https://doi.org/10.1180/mgm.2021.43.
Westrich, J.T., Berner, R.A., 1984. The role of sedimentary organic matter in bacterial sulfate reduction: The G model tested. Limnol. Oceanogr. 29, 236–249.
Whitney, D.L., Evans, B.W., 2010. Abbreviations for names of rock-forming minerals. Am. Mineral. 95 (1), 185–187. https://doi.org/10.2138/am.2010.3371.
Whittig, L.D., Allardice, W.R., 1986. X-Ray diffraction techniques. In: Klute, A. (Ed.), methods of soil analysis, Part 1: Physical and mineralogical methods. American Society of Agronomy, Madison, pp. 331–362.
Williams, L.A., Parks, G.A., Crerar, D.A., 1985. Silica diagenesis, I. Solubility controls. J. Sediment. Petrol. 55 (3), 301–311. https://doi.org/10.1306/212f86ac-2b24-11d7-8648000102c1865d.
Winsauer, W.O., McCardell, W.M., 1953. Ionic double layer conductivity in reservoir rock. J. Petrol. Technol. 5 (5), 129–134. https://doi.org/10.2118/953129-G.
Worden, R.H., Morad, S., 1999. Clay minerals in sandstones: Controls on formation, distribution and evolution. https://doi.org/10.1002/9781444304336.ch1.
Worden, R.H., Smalley, P.C., Barclay, S.A., 2003. $H_2S$ and diagenetic pyrite in North Sea sandstones: Due to TSR or organic sulphur compound cracking? J. Geochem. Explor. 78–79, 487–491. https://doi.org/10.1016/S0375-6742(03)00072-4.
Wright, V.P., Barnett, A.J., 2020. The textural evolution and ghost matrices of the Cretaceous Barra Velha formation carbonates from the Santos Basin, offshore Brazil. Facies 66 (1), 7. https://doi.org/10.1007/s10347-019-0591-2.
Wyllie, M.R.J., Southwick, P.F., 1954. An experimental investigation of the SP and resistivity phenomena in dirty sands. J. Petrol. Technol. 6 (2), 44–57. https://doi.org/10.2118/302-G.
Xu, S., Hao, F., Xu, C., Zou, H., Gao, B., 2019. Seismic geomorphology and sedimentology of a fluvial-dominated delta: Implications for the Neogene reservoirs, offshore Bohai Bay Basin, China. AAPG Bull. 103 (10), 2399–2420.
Zhang, S., Xu, Y., Lu, P., 2022. Analysis and modelling of dolomite sealing potential. Petrol. Chem. Indus. Int. 5 (3), 153–161.
Zhu, C., Cui, X., He, Y., Kong, L., Sun, Y., 2020. Extended 3$\beta$-methylhopanes up to C45 in source rocks from the Upper Cretaceous Qingshankou Formation, Songliao Basin, Northeast China. Org. Geochem. 142, 103998. https://doi.org/10.1016/j.orggeochem.2020.103998.